Geochemistry of target rocks, impact-melt particles and metallic spherules from Meteor Crater, Arizona: Empirical evidence on the impact process[†]

David W. Mittlefehldt[1*], Friedrich Hörz[1], Thomas H. See[2], Edward R.D. Scott[3] and Stanley A. Mertzman[4]

[1]SR, NASA/Johnson Space Center, Houston, TX 77058, USA
[2]C23, Lockheed Martin SO, 2400 Nasa Rd. 1, Houston, TX 77058, USA
[3]Hawai'i Institute of Geophysics and Planetology, University of Hawai'i, Honolulu, HI 96822, USA
[4]Dept. of Geosciences, Franklin and Marshal College, Lancaster, PA 17604, USA

[*]Corresponding author's e-mail address: david.w.mittlefehldt@nasa.gov

[†]This paper is dedicated to the memory of David J. Roddy, field-guide, colleague and friend.

Geological Society of America
Special Paper – Large Meteorite Impacts
submitted: 25 November 2003

ABSTRACT

We have done lithophile- and siderophile-element analyses of target rocks, and ballistically dispersed impact-melt particles and metallic spherules from Meteor Crater, AZ. The upper Moenkopi Formation has a unique lithophile-element signature that confirms it as a major component of the impact-melt particles. The Kaibab Formation is very heterogeneous, containing dolomite-rich and quartz-rich layers. The lithophile-element compositions of the impact-melt particles can be entirely explained as mixtures of Moenkopi and Kaibab depleted in CO_2. The Toroweap and Coconino Formations are not required components, but small contributions from them are not excluded. We conclude the impact-melt particles were formed in the upper portion of the section, above the sandstone units.

The impact-melt particles on average contain about 14% Canyon Diablo meteorite material. Most siderophile-element ratios of the impact-melt particles are unchanged from those of the projectile. Many samples are depleted in Au, with the most extreme depletions found in impact-melt particles with the highest Kaibab component. Because Kaibab rocks are higher in Br than other target rocks, we suggest loss of volatile Au halides may have caused the fractionation.

Ballistically dispersed metallic spherules are enriched in Co, Ni, Ir and Au compared to Canyon Diablo metal. Element/Ni ratios deviate slightly from Canyon Diablo ratios, and are inversely correlated with oxidizability. We attribute this to partial oxidation of molten metal spherules during flight. Spherule compositions suggest slight selective melting of graphite-troilite-schreibersite inclusions of the projectile consistent with enhanced shock melting of these lower density inclusions.

"Special features, such as the presence of layering or volatiles in the target are not shown here. The effects of such circumstances are largely unknown at present."

H.J. Melosh

Impact Cratering. A Geologic Process, p. 48

INTRODUCTION

In support of the push to put a man on the moon in the 1960s, planetary sciences underwent a period of vigorous growth. One result of this was the recognition that impact processes play an important role in modification of the surfaces of planetary bodies. All solid surfaces in the solar system are scarred by impacts, from Mercury, to the moons of Neptune. In addition, impact melts, melt breccias, regolith breccias and shock-damaged rocks are common among the returned lunar samples and almost all meteorite types.

The study of impact processes has generally progressed along a five pronged front: (i) field and petrologic study of terrestrial impact craters and their products, (ii) laboratory-scale impact experiments, (iii) large-scale explosion experiments, (iv) theoretical modeling of the impact process, and (v) astronomical and spacecraft study of craters on planets, moons and asteroids (see Melosh, 1989). Geochemical studies generally have contributed to the identification of a meteoritic signature in impact melts (e.g., King et al., 2002), attempted to identify the type of impactor (Morgan et al., 1975; Palme et al., 1978), or established the process of mixing of target rocks to form unusual impact-melt rocks (e.g., Dence, 1971; Grieve, 1982; Simonds et al., 1978). Chemical studies aimed at a more detailed understanding of the cratering process have been limited for several reasons. Older structures have been eroded and/or buried, making detailed reconstruction of the pre-impact chemical stratigraphy difficult. Impact-melt sheets in larger structures may have suffered hydrothermal alteration (see Hagerty and Newsom, 2003), which may have altered the composition of the melt sheet. Finally, older and larger

structures generally do not have preserved meteoritic material available for study (Grieve, 1991), so the type of impactor cannot be confidently identified. As a consequence, the depth of the melt zone is poorly defined, and there are substantial uncertainties regarding the degree of fractionation of impactor and target rocks during melting.

Recently, studies have been done on a few younger, smaller impact craters for which projectile material is also available. Attrep et al. (1991) presented the results of the geochemical study of a limited number of samples from Henbury and Wolfe Creek Craters. These authors showed that siderophile-element ratios in "impactites" are fractionated relative to those of the preserved projectile material. We did an extensive study of samples from Wabar Crater that confirmed that siderophile-element fractionations occurred during formation of impact-glass particles (Mittlefehldt et al., 1992). We further suggested that because lithophile elements were not fractionated in the glasses, fractionation of the siderophile elements must have occurred before mixing of the projectile and target materials. We also inferred that projectile material was preferentially mixed with the upper stratigraphic horizons of the target.

We have continued our study of natural impacts through field, petrologic and geochemical study of Meteor Crater, Arizona, the largest crater with associated preserved projectile material (Grieve, 1991). Meteor Crater is almost an ideal candidate for such study as the stratigraphy is variegated, allowing a more detailed look at the projectile-target interaction; it is young and fresh; abundant impact-melt material already resides in collections and is easily obtained for study; and remnants of the projectile have been well characterized. We have pursued a number of studies in our effort to understand the impact process at Meteor Crater. The results of our detailed study of the mineralogy and major-element chemistry of the target rocks and the petrology of the impact glasses have been reported (Hörz et al., 2002; See et al., 2002).

Here we present our completed study of lithophile and siderophile elements for target rocks, impact-melt particles, and metallic spherules.

GEOLOGIC SETTING AND BACKGROUND

Pre-impact target

Meteor Crater is one of the best-studied terrestrial impact structures, and the detailed pre-impact stratigraphy and structure are well known. The synopsis given here is taken from Roddy (1978), Roddy et al. (1975) and Shoemaker (1963; 1987). See et al. (2002) presented details of the major-element chemistry and mineralogy of a stratigraphic sequence systematically collected from the crater walls. These references should be consulted for detailed discussion of the target rocks.

Meteor Crater was formed in a generally flat-lying sequence of Mesozoic and Paleozoic sediments. The uppermost unit, the Triassic Moenkopi Formation, consists of calcareous sandstone and siltstone. This unit is patchy and varies considerably in thickness from about 1 to 24 m near the crater, but is estimated to have averaged ~8.5 m in thickness in the area destroyed by the impact (see Roddy, 1978). In the crater walls, the Moenkopi systematically varies from more carbonate-rich at the top to more quartz-rich at the bottom (See et al., 2002). Below the Moenkopi is the Permian section starting with the Kaibab Formation, an approximately 80 m thick carbonate sequence consisting largely of sandy dolomite, but including some sandstone. The composition of this unit is highly variable reflecting wide ranges in quartz and dolomite content; calcite is a minor component. The upper half of the unit is richer in carbonate than is the lower half (See et al., 2002). Below the Kaibab is the thin, ~1.5 m thick Toroweap

Formation consisting dominantly of dolomitic sandstone. The bottom of the crater is in the ~220 m thick Coconino Formation which is composed of very pure sandstone with SiO_2 contents >95 wt%. Below the Coconino is the Permian Supai Formation of sandstone and siltstone. The Supai is believed to be brecciated, but there is no evidence that the transient crater excavated it.

Canyon Diablo iron meteorite

Meteor Crater was formed by the impact of the Canyon Diablo IAB iron meteorite, which is estimated to have been ~33 m in diameter for an assumed impact velocity of 15 km/sec (Roddy, 1978). The IAB group is one of the non-magmatic iron meteorite groups, so-called because their chemical characteristics are not those of metal formed by fractional crystallization of a metallic core (Scott and Wasson, 1975). The IAB irons, especially Canyon Diablo, have been extensively studied. Wasson and Ouyang (1990) have done a detailed compositional study of Canyon Diablo, while Choi et al. (1995) have presented a thorough study of the composition of the metal phase of most IAB irons. Choi et al. (1995) present an average composition of Canyon Diablo based on 64 analyses, which we use here in discussions of our siderophile-element data for impact-melt particles and metallic spherules. The composition of the Canyon Diablo iron, with 70 mg/g Ni, is typical of that of the majority of IAB irons.

Buchwald (1975) gave a detailed description of the petrology of Canyon Diablo and most other IAB irons. It is a coarse octahedrite containing about 8.5% by volume of troilite-graphite inclusions. These inclusions have varying ratios of troilite to graphite, and include a suite of minor phases. They are typically surrounded by schreibersite and cohenite (Benedix et al., 2000; Buchwald, 1975). Buchwald (1975) estimates that on average, the inclusions have roughly equal amounts of troilite and graphite by volume. Silicate inclusions are present in many members of

the IAB group (e.g., Benedix et al., 2000; Mittlefehldt et al., 1998). Although not commonly seen in Canyon Diablo specimens, Buchwald (1975) reports that silicates are present in some troilite-graphite nodules. The silicates in IAB irons are mostly chondritic in composition, although other types also occur (Benedix et al., 2000; Bunch et al., 1970).

Meteor Crater and impact products

Meteor Crater is a classic bowl-shaped impact crater approximately 1 km in diameter, although structural controls in the rocks in the target area give it a squarish shape in map view (Roddy, 1978). The crater was formed approximately 50 Ka ago (Nishiizumi et al., 1991; Phillips et al., 1991). Shocked and frothy Coconino sandstone occurs in the crater floor below a layer of alluvium, but no continuous impact-melt sheet is present (Roddy et al., 1975). Shocked and brecciated target rock occurs on the crater floor, in the walls and in the overturned flap (Roddy et al., 1975). Impact melt composed of mixtures of target rock and projectile are confined to particles up to a few cm in size ballistically dispersed over the plains surrounding the crater (Nininger, 1956). Metallic spherules a few mm in diameter are also found on the surrounding plains (Nininger, 1956). These are melt-droplets of the Canyon Diablo iron and are not mixed with target rock (Blau et al., 1973). Finally, some samples of Canyon Diablo show petrographic evidence for shock deformation superimposed on the normal structure of the iron. These are solid fragments of the impactor spalled from the backside of the projectile as the shock wave reflected off the free surface (Buchwald, 1975).

SAMPLES AND ANALYTICAL METHODS

Samples

We have analyzed three types of materials for this study: (i) representative samples of the target rock, mostly from within the crater or the overturned flap, (ii) ballistically dispersed impact-melt particles, and (iii) metallic spherules. A few of the target-rock samples analyzed during the initial stages of this study were collected solely as representative hand samples of the Kaibab and Coconino Formations, and are from undocumented locations. A second set of documented samples from within and around the crater was collected specifically to obtain a representative suite of the lithologic diversity within the crater. Brief descriptions of these samples are given in Appendix 1. A third set of samples was collected specifically to obtain a measured stratigraphic sequence from within the crater for geochemical and mineralogical characterization. The samples, major-element analyses by x-ray fluorescence (XRF), and mineralogy determined by x-ray diffraction (XRD) of these are given in See et al. (2002). The impact-melt particle and metallic spherule samples were obtained from the collection of the Center for Meteorite Studies, Arizona State University. H.H. Nininger collected these samples from the plains surrounding the crater, but their precise collection locations are not known. The impact-melt particles were selected by one of us (FH) to represent the range of materials in the collection. Brief macroscopic descriptions of these are given in Appendix 2. The petrology of the impact-melt particles has been discussed in detail in Hörz et al. (2002).

Analytical methods

The target-rock and impact-melt particle samples were analyzed by instrumental neutron activation analysis (INAA) at Johnson Space Center (JSC) in a series of irradiations. Some of the target rocks, those labeled Ma, Ka, Ta, Ca, etc., are splits of the pooled "subsection" samples of See et al. (2002). For the other target rocks, several grams of each sample were ground and

homogenized, and splits taken for analysis. Some of the impact-melt particles contained variable amounts of adhering alteration material, or fine-grained alluvial or soil particles. These contaminants were removed by scraping with a dental pick and ultrasonication in distilled water. The impact-melt particles were then coarsely crushed and the cleanest impact-melt material was handpicked from among the larger fragments. Many of the impact-melt particles are finely vesicular, and alteration material was found even in interior vesicles. It proved impossible to eliminate all of the alteration material. The occurrence of alteration material even in tiny interior vesicles indicates that it likely formed from elements leached out of the glass. Samples of alteration material from three impact-melt particles were analyzed in order to evaluate the potential effects of this material on analyses. For the larger impact-melt particles, clean material was crushed and homogenized and splits taken for INAA. For the smaller particles, the entire clean sample was used for INAA.

The samples, standards and international standard rocks used as controls were sealed in ultra-pure silica glass tubes, and irradiated at the University of Missouri Research Reactor Facility. The samples were counted three or four times at differing times after irradiation to obtain data for nuclides of differing half-lives. Irradiation times, neutron fluxes and counting schedules were slightly different for the different irradiations depending on the nature of the total sample package. Data reduction was done using standard JSC procedures (Mittlefehldt and Lindstrom, 1991, 1993). The impact-melt particles and some target rocks have high Mg contents and low Na contents. A correction to the data was applied to account for Na produced by (n,p) reactions on Mg. The ultra-pure silica contains a tiny amount of La that can significantly affect the data for very small or La-poor samples. A blank correction was made as needed.

The metallic spherules were analyzed by INAA at UCLA in the mid 1970s. The samples consisted of metal cores with oxide coatings. Following Kelly et al. (1974), the samples were abraded in a mixer-mill with a sandpaper lining until the oxide coatings appeared to have been removed. The spherule samples, six samples of the North Chile hexahedrite (IIA iron) Tocopilla serving as standards, and the IVA iron meteorite Rembang serving as a control, were irradiated at the Ames Laboratory Research Reactor at a flux of $2x10^{13}$ n cm^{-2} sec^{-1} for 10 hours, and counted several times to obtain data for elements of differing half-lives. Subsequently, four of the samples were reirradiated at the UCLA reactor for radiochemical determination of Ga and Ge following the procedures of Wasson and Kimberlin (1967).

Splits of the larger impact-melt particles were fused to glass on a Mo metal strip in an Ar atmosphere following the procedure of Brown (1977) and major elements were determined by electron microprobe analysis (EMPA). This procedure was designed for use with basaltic compositions, and the unusual compositions of the impact-melt particles caused two problems. First, the impact-melt particles are not in internal equilibrium, especially with respect to oxidation state – they contain Fe^{3+}, Fe^{2+} and Fe^{0} (see Hörz et al., 2002). Because of this, Mo from the strip was oxidized and dissolved in the glass at up to a few wt% in the most extreme cases. Some of the Fe remained in the metallic state, and thus, was not part of the homogeneous glass. For this reason, there is poor agreement between FeO determined by INAA and EMPA. However, the major-element data are used to determine which of the target rocks contributed to the impact-melt particles. The target rocks are generally poor in FeO, and most of the Fe in the impact-melt particles is derived from the impactor (See et al., 2002; this study). To first order, FeO can be ignored in evaluating target-rock contributions to the impact-melt particles. The

glass beads were analyzed with the JSC SX100 electron microprobe using a 15kV potential, 15 nA sample current, and the electron beam rastered over a 10x10 μm area.

See et al. (2002) presented major-element analyses by XRF of many of the target rocks studied here. Additional target-rock samples plus a composite of 15 impact-melt particles were analyzed as part of this study. The analytical methods follow standard procedures used at Franklin and Marshal College, described in detail by Boyd and Mertzman (1987). An exception to these procedures is that the samples were first ground and homogenized in an agate mortar and pestle at JSC, and splits sent to Franklin and Marshall College for analysis. Final grinding and sieving were done at Franklin and Marshall. Major-element contents were determined by XRF analysis, with all Fe determined as Fe_2O_3. The ferrous iron content was determined by titration, and loss on ignition was determined by heating an aliquot at 950°C for one hour.

RESULTS

The results of our analyses are presented in Tables 1-5. Table 1 presents the major-element analyses of the target rocks plus the composite impact-melt particle (H11). The XRF analysis determines major elements on a volatile-free basis, and all Fe as Fe_2O_3. In Table 1 the data have been recast to a volatile-bearing basis, and with Fe split between FeO and Fe_2O_3 as determined by titration. The low sum for the analysis of the composite impact-melt particle is an artifact of the recalculation. It has a high total Fe content, with much of it ferrous – the XRF sum was 99.31. The INAA data on target rocks, including those studied by See et al. (2002) are given in Table 2. Our INAA data on impact-melt particles are given in Table 3, and major-element analyses of select impact-melt particles determined by EMPA on fused beads are presented in Table 4. These latter analyses are normalized to sum 100%. As mentioned, the

analyses included variable amounts of MoO_2 (<0.01 to 4.56 wt%) derived from the strip heater, and the Fe in the glass likely is a mixture of FeO and Fe_2O_3. These analyses are primarily used to evaluate which of the target rocks dominate in the impact-melts, and devolatilized, Fe-free (projectile-free) compositions are needed for this evaluation. Table 5 contains our INAA data on the metallic spherules. We have also done INAA on a few miscellaneous samples from the impact-melt particle suite – a lithic clast, samples of secondary alteration products and an oxide bead. These data are given in Appendix 3 for completeness.

DISCUSSION

There are several problems associated with comparing geochemical data on the target rocks with those on impact-melt particles. The high-temperature formation of the impact-melt particles caused devolatilization of carbonates and hydrous phases of the target components, and mixing of projectile material into the impact-melts diluted the target components. Because of this, when comparing the compositions of target rocks and impact-melt particles, we use normalized compositions. The impact-melt particle compositions are normalized to Fe-Ni-Co-free basis. The volatile content of these particles is not known, but they should be nearly volatile-free. We arbitrarily use the LOI determination on the composite of 15 impact-melt particles (H11, Table 1) to correct for volatile content. The target-rock compositions are normalized to a volatile-free basis using the LOI determinations, and to an iron-free basis to make them more directly comparable to the impact-melt particles. These corrected impact-melt and target-rock compositions are referred to as “adjusted” compositions.

The data on impact-melt particles given here are not directly comparable to the impact-melt glass compositions reported by Hörz et al. (2002). The latter are for EMPA of glasses,

while the data presented here are for bulk particles, including glass, quenched mineral phases, undigested clasts and remnant metal and sulfide beads.

Geochemical stratigraphy of Meteor Crater

Previously, we established that the upper portion of the target stratigraphy shows substantial major-element compositional heterogeneity (Hörz et al., 2002; See et al., 2002). The Moenkopi Formation shows a general decrease in CaO and LOI, and an increase in SiO_2 from top to bottom, indicating increasing quartz sand and decreasing calcite with depth. The Kaibab exhibits substantial fluctuation in SiO_2 and MgO+CaO throughout the section reflecting variations in quartz sand and dolomite. On a finer scale, we found that the quartz content of the Kaibab varies from almost 100% to ~15% within the section (Hörz et al., 2002; See et al., 2002). These variations are non-systematic – the Kaibab sample with the lowest quartz content is from immediately above a sample with one of the highest (see Hörz et al., 2002, Fig. 15, samples K106.2 and K104.7). The Toroweap and Coconino are distinguishable from other target rocks only by their high SiO_2 contents.

Variations in adjusted major-element content of the target rocks with depth in the crater are shown in Fig. 1. The Moenkopi is distinct in having much higher Ti and Al contents than all other units, while the Kaibab is distinct in having a much higher Mg content, and generally lower but variable Si content. The non-systematic variation in Si in the Kaibab shows up in the depth profile (Fig. 1). The high Al content of the Moenkopi indicates a higher terrigenous component (e.g., clays) in it than in other units in the section. This is also seen in trace-element contents (Fig. 2). The Moenkopi is rich in Sc, the rare-earth elements and Ta compared to the other units. The two lowest samples from the Moenkopi also are rich in Hf, but the upper portion has Hf

contents like those of the Kaibab. The Kaibab is distinct in showing a general increase in U content with depth, and the lower portion of the section has the highest U content in the depth profile (Fig. 2).

The Toroweap and Coconino are lower in all major and trace elements measured when adjusted to a volatile- and iron-free basis, excluding Si (Figs. 1, 2). Hence, these units would only act as diluents in lithophile-element mixing relations should they be a component of the impact-melt particles.

Lithophile elements and target rock mixing

Kargel et al. (1996) suggested that impact-melt particles from Meteor Crater are composed of mixtures of projectile and rock from the Kaibab Formation, with no clear signature for either Moenkopi or Coconino rocks in the mix. Our preliminary synopsis of the compositions of target rocks and impact-melt particles led us to suggest that the Moenkopi and Kaibab strata are the primary terrestrial components in the impact-melt particles (Mittlefehldt et al., 2000). This was supported by our modeling of the major-element compositions of glasses contained in the impact-melt particles. We identified three distinct melt compositional types and concluded that different mixtures of Moenkopi and Kaibab components could explain the glass compositions, with Moenkopi composing as much as half of the target component in some glasses (Hörz et al., 2002). While we could not exclude Coconino as a minor component of some glasses, the data do not require it. We suggested that the melt zone was a relatively small fraction of the transient crater volume, and that melting occurred at depths of <30 m for many, and possibly all, of the glasses (Hörz et al., 2002).

Mixing relations for major elements between target rocks and bulk impact-melt particles are shown in Fig. 3. All impact-melt particles in the three binary systems shown – Mg-Al, Ca-Al and Ti-Si –fall within a field defined by Moenkopi and Kaibab samples. No impact-melt particles have excesses in Si or deficits in the other elements that would require addition of Toroweap/Coconino into the mix. However, the scatter in the data would *permit* a small Toroweap/Coconino component. In the Mg-Al plot, we show an expansion of the central portion of the impact-melt field demonstrating that the data range could obscure at most about a 10% contribution by Coconino to the impact-melts. Because there are no distinguishing elements in the Coconino or Toroweap, they are difficult to fingerprint in the impact melts.

Lithophile-trace-element contents of impact-melt particles and target rocks are in accord with the inference made from major-element contents. In Ca-Sc and Ca-Ta plots, the impact-melt particles plot between the fields occupied by Kaibab and Moenkopi rocks, and away from the trace-element-poor Toroweap and Coconino (Fig. 4). The Toroweap and Coconino rocks have the lowest lithophile-trace-element contents (Table 2, Fig. 2), and the lithophile-trace elements are generally correlated in the target rocks. Because of this, on diagrams such as Ta vs. Sc (Fig. 4), Toroweap and Coconino rocks could be interpreted as one end member of a mixing trend. However, their stratigraphic location argues against this. The Ta-Sc plot clearly shows that the topmost unit, the Moenkopi, is a significant component of the impact-melts, and that all of them lie between the fields for Moenkopi and Kaibab rocks. Because the Kaibab is a thick unit between the Moenkopi and Toroweap/Coconino, it is more plausible that the Kaibab is the most significant trace-element-poor component in the impact-melts.

The lithophile-element contents of some impact-melt particles are outside the ranges for Moenkopi and Kaibab rocks. For example, the adjusted La content of a few are higher than

observed in our suite of Moenkopi rocks, while the U and K contents of many are lower than those of the Kaibab or Moenkopi rocks (Fig. 5). The high La contents determined for a few impact-melt particles relative to Moenkopi rocks likely indicates that our sampling of this formation at ~2.5 meter scale was inadequate to define the effective compositional heterogeneity of the formation.

The low K and U contents for many of the impact-melt particles suggest possible element fractionation during or after their formation. Potassium and the other alkali elements potentially could have been partially volatilized during the high temperature phase. Uranium is normally considered a refractory element, but some U halides are quite volatile (Lide, 2001). The Kaibab formation typically contains 1-2 µg/g Br (Table 2) and likely much higher contents of Cl (seawater Cl/Br ~290). Hence, formation and loss of species such as UCl_4 (boiling point 1064°K, Lide, 2001) may have occurred. Alternatively, the low K and U contents might indicate loss during low-temperature alteration of glasses in the particles. We documented late oxidation of Fe in glasses (Hörz et al., 2002), and vesicles in the interiors of some impact-melt particles contain secondary phases indicating leaching from the particles. Uranium is subject to oxidation and mobilization during alteration, and alkali elements are typically easily mobilized during alteration. Regardless, the K and U contents of the impact-melt particles do not indicate that Toroweap or Coconino are significant components. Those impact-melt particles with the lowest K and U contents, like those of Toroweap and Coconino rocks, nevertheless contain high Ca contents demonstrating a large Kaibab component.

Based on the major-element compositions of glasses in impact-melt particles, we concluded that mixing rocks from the upper 30 m of the target formed some of them (Hörz et al., 2002). We have not attempted to do formal mixing calculations based on the major- and trace-

element data for bulk impact-melt particles presented here, but our earlier conclusion is compatible with them. We also concluded that while the higher SiO_2 contents of some of the glasses *may* indicate a small component of Coconino is present, this was not *required* by the data. As shown in Fig. 3, the major-element contents of the impact-melt particles would allow for as much as ~10% Coconino. However, because all major- and trace-element data (excluding potentially mobile elements such as K and U) for the impact-melt particles lie between the fields for Moenkopi and Kaibab, we believe it to be more plausible that only these two rock units were mixed in the melt zone to form the particles, and thus the melt zone extends no deeper than the base of the Kaibab, ~85 m at most.

Siderophile elements and projectile-target mixing

The impact-melt particles contain a substantial projectile component. The siderophile-element contents normalized to the mean Canyon Diablo metal composition (Choi et al., 1995) show that Co, Ni and Ir contents reach 22-27% of that of the projectile (Fig. 6). However, because CO_2 was volatilized from the carbonate-rich target rocks, the actual maximum projectile component mixed with the bulk target is less. There is a fairly good correlation between target-rock CaO+MgO and LOI (See et al., 2002), and we have used this to estimate the mass of target rock lost during impact melting for those particles for which we have major-element data (Table 4, plus H11, Table 1). For these we estimate that between 7-15% of the mass was lost, and that the maximum projectile component based on Co, Ni and Ir was thus between 20-22%. Using an average mass correction of 11%, we find that the impact-melt particles contain, on average, 14% projectile component. This is higher than we found for ballistically dispersed impact-melt particles from Wabar Crater (Fig. 6). There we found average projectile components of ~7% and

~9% for large and small glass beads, with a maximum of ~17% for one small bead (Mittlefehldt et al., 1992).

There are very few other craters where both impact melts and impactor are preserved, and very few analyses of impact melts have been done. Attrep et al. (1991) found projectile components of ~4% and ~10% (based on Co and Ni) for two impact melts from Wolfe Creek Crater (Fig. 6), and <1% for three impact melts from Henbury Crater. The types of impact melts analyzed from these two craters were not specified. The very low projectile component in the Henbury Crater samples most likely indicates that they represent massive-melt objects. We previously showed that large melt specimens (>100 g) from Wabar contain a much smaller projectile component than do ballistically dispersed, mm-sized melt beads (Mittlefehldt et al., 1992). The Henbury samples will not be discussed further.

The Meteor Crater impact-melt particles have relatively unfractionated Co/Ni and Ir/Ni ratios over the range of projectile contents, but Au is strongly fractionated as exemplified by Au/Ir ratios (Fig. 6). The Au fractionation is independent of the amount of projectile component in the particles. Samples with projectile-normalized Au/Ni ratios as low as 0.03 have normalized Co contents ~20% that of the Canyon Diablo iron, and two samples with normalized Au/Ni of 0.82 and 0.90 have normalized Co contents of 7% and 10% that of the projectile (Fig. 7). This shows that the Au fractionation is independent of the target-projectile mixing process, i.e., fractional condensation from a vapor cloud or selective vaporization from the impact melts of siderophile elements is not the cause (see Kelly et al., 1974 and Gibbons et al., 1976 for discussions of proposed fractionation processes). This is also suggested by hydrocode simulations of the Meteor Crater impact that show that for plausible impact velocities, projectile vaporization is unimportant (Schnabel et al., 1999).

Two samples have anomalous siderophile-element characteristics. Particle M20 has high Co/Ni and Ir/Ni ratios due to depletion in Ni – increasing Ni by a factor of 2.5 brings this sample within the range of other impact-melt particles for Co/Ni and Ir/Ni. Particle M20 contains clear glass and two types of altered glass intimately mixed (Hörz et al., 2002). The clear glass contains ~7% projectile component, and has an Fe/Ni ratio like that of the projectile, while the altered glasses are very iron-rich with Fe/Ni ratios much greater than that of the Canyon Diablo iron (Hörz et al., 2002). The bulk sample studied here is like the clear glass in Fe content, but like the two types of altered glass in Na, K and Ca. Possibly, the anomalous characteristics of M20 may simply reflect heterogeneous distribution of the siderophile elements among different glass types. Particle M12 has a very low Ir/Ni ratio due to an anomalous Ir content. This particle has a Au/Ir ratio like that of the Canyon Diablo iron, but this is anomalous compared to all other impact-melt particles with low Ir and Au contents (Fig. 6). Particle M12 contains only clear glass, with the lowest projectile component among those studied (Hörz et al., 2002). This is also observed in the bulk impact-melt particle, with ~3.5% projectile based on Co and Ni. Note however that the Ir and Au contents are much lower and suggest only ~0.1% impactor (Fig. 6).

The siderophile-element characteristics of the Meteor Crater impact-melt particles show some similarities and some differences with those from Wabar and Wolfe Creek Craters (Fig. 6). Most Wabar samples have Co/Ni ratios significantly elevated above that of the impactor, while only Meteor Crater particle M20 is so endowed. The single Wolfe Creek Crater sample plots close to the impactor line – more data are required to determine whether Co/Ni fractionation occurred at this crater. Most Wabar impact-melt particles have Ir/Ni ratios like that of the impactor. A few have anomalously low Ir/Ni ratios, but none are as anomalous as M12. Both

Wolfe Creek Crater samples show anomalous Ir/Ni ratios, but again, not to the extent of M12. All samples from Wabar Crater and the single sample from Wolfe Creek Crater have Au/Ir ratios less than that of the projectile. Although only three craters have been sampled, and for one only a single sample was analyzed, the data suggest Au fractionation may be a common process occurring during impact melting at terrestrial craters.

Attrep et al. (1991) and we (Mittlefehldt et al., 1992) stated that observed siderophile-element fractionations in terrestrial impact melts indicate that attempts to identify impactor types from analyses of impact melts from the Earth and Moon should be treated cautiously. We still believe this to be true for terrestrial craters. However, the observed fractionations may be uniquely terrestrial, and thus, may not apply to impact melting on the Moon. There is general tendency for those Meteor Crater impact-melt particles with the highest molar (Ca+Mg)/Si to have lower normalized Au/Ir ratios (Fig. 8), indicating that those with a higher Kaibab component are more fractionated. Among the target rocks, Kaibab samples have generally higher Br contents (Fig. 8), and Se, a proxy for S, was detected almost exclusively in Kaibab Formation rocks (Table 2). This suggests that the Au fractionation is tied to the volatile content of the target, and that volatile Au complexes may have been formed and lost during impact melting. If true, then siderophile-element fractionation may not occur during impact melting on the Moon.

Unfortunately, the case is not clear-cut. There is substantial scatter in the Meteor Crater data (Fig. 8) that obscures compositional correlations. This may result from the heterogeneous nature of the Kaibab (Figs. 1, 2; Hörz et al., 2002; See et al., 2002), the heterogeneous melting process, or that the trend is not real. Wolfe Creek Crater was formed in Precambrian quartzite, and we have no detailed information on the composition of the target rocks. Wabar Crater was

formed in sandstone and the low Ca contents of Wabar impact glasses and target materials indicate that there was little carbonate in the target (Hörz et al., 1989; Mittlefehldt et al., 1992). We do not have Br or Se data for the Wabar target-rock samples, and thus, cannot compare possible halogen or sulfate contents with Meteor Crater. More data on target rocks and impact-melt particles from additional craters in which the projectile has been preserved are needed to evaluate the cause of Au fractionation observed in impact-melt particles from terrestrial craters.

In our study of Wabar impact-melt particles, we deduced that more projectile material was mixed into melts formed in the upper portions of the melt zone than in the lower portions (Mittlefehldt et al., 1992). The Meteor Crater data give some support to this. The Kaibab rocks have the highest molar (Ca+Mg)/Si and (Ca+Mg)/Al ratios in the target stratigraphy (Fig. 9). These ratios should then increase in impact-melt particles formed as the melt zone penetrates deeper into the section. Impact-melt particles with (Ca+Mg)/Si and (Ca+Mg)/Al ratios less than in any of the Kaibab rocks have projectile-normalized Ir contents that are, on average, higher than those with the highest (Ca+Mg)/Si and (Ca+Mg)/Al ratios (Fig. 9). Remember that the impact-melt particles have had their projectile component enhanced through mass-loss of CO_2 during melt formation, and that samples with higher (Ca+Mg)/Si ratios (higher carbonate component) have lost the most mass. Thus, the normalized Ir contents of those samples on the right side of Fig. 9 have been enhanced systematically more by this process than those on the left. The data are broadly consistent with a generally decreasing projectile/target mixing ratio as the projectile penetrates the target. Samples with the highest normalized Ir contents have intermediate (Ca+Mg)/Si (~0.5-0.6) and (Ca+Mg)/Al (~7-8) ratios (Fig. 9), possibly indicating that the peak projectile/target mixing ratio was reached at some intermediate depth in the melt zone, rather than at the target surface.

Two impact-melt particles, M12 and M20, have lithophile-element contents indicating a higher Moenkopi component, yet have very low Ir contents (Fig. 9). These run contrary to the general argument just made regarding a greater projectile component in impact-melt particles formed higher in the section. Both of these samples were small, and no material remained for major-element analyses; the data plotted are based on clear glass analyses of Hörz et al. (2002). These authors inferred that the M12 and M20 glasses contained a higher Moenkopi component than most clear glasses analyzed, and that their low FeO contents indicated a low projectile component. Our INAA data for K, Ca and Fe on bulk M12 match well the probe data for clear glass (Hörz et al., 2002, Table 3) suggesting that most of the bead was composed of such glass. As discussed above, M12 has anomalous siderophile-element contents, with Co and Ni indicating 35 times more projectile material than indicated by Ir and Au. The bulk data for M20 do not match the glass data very well. Bulk particle M20 has by far the lowest CaO content of any of the impact-melt particles (Table 3), yet the clear glass has among the highest CaO contents (Hörz et al., 2002, Table 3). Altered glass in M20 has much lower CaO contents (Hörz et al., 2002), similar to what we found for the bulk particle. However, the altered glass has much higher Fe contents than the clear glass, and our bulk particle datum matches the clear glass in Fe. Clearly, a simple understanding of the relationship between bulk M20 and the glasses it contains is elusive. M20 also has somewhat anomalous siderophile-element contents (Fig. 6). Thus, M12 and M20 should be treated cautiously when attempting to infer projectile-target mixing details.

There are two impact-melt particles for which we have major-element compositions determined on fused beads for comparison with the clear glasses of Hörz et al., 2002) – M18 and SIG-4 (Fig. 9). Bulk SIG-4 has (Ca+Mg)/Al and (Ca+Mg)/Si very similar to those of the clear glass. We did not note clastic material in this sample, and the data are consistent with the bulk

of the particle being similar to the clear glass. Bulk M18 is very different from its clear glass in major-lithophile-element contents (Fig. 9). The bulk sample contains higher CaO and MgO than does the clear glass, suggesting incorporation of dolomite clasts in the bulk particle. This then implies additional Kaibab component not recorded in the clear glass composition. Thus, it is difficult to determine whether M18 violates the projectile-target mixing generalization discussed above.

One last point regarding comparing our earlier results on glasses with the bulk particles studied here needs to be stressed. Hörz et al. (2002) showed that there are two basic types of glasses in the impact-melt particles, those with low Fe and Ni, and Ni/Fe like that of the projectile, and those with high Fe, low Ni and Ni/Fe much lower than that of the projectile. In contrast, the bulk particles have essentially a continuum of Fe contents covering the total range observed in the glasses, but all have Ni/Fe like that of the impactor. Thus bulk impact-melt particles have variable contents of unfractionated (except for Au) projectile material. Some glasses on the other hand, contain a fractionated projectile component that must be compensated by other phases, probably metal or sulfide blebs, contained in the bulk particle. Electron microprobe analyses of metal blebs in impact-melt particles show that they can be highly enriched in Ni and Co relative to Canyon Diablo metal (Brett, 1967; Kelly et al., 1974; our unpublished data), and can balance the low Ni contents observed in high-Fe, low-Ni glasses observed by Hörz et al. (2002).

Metallic spherules and melting of the projectile

Blau et al. (1973) studied the textures and compositions of a suite of metallic spherules from Meteor Crater. They stated that the dendritic texture demonstrated that the spherules

solidified from a molten alloy, limiting permissible models to those involving quenching of liquid droplets. They noted that the textures of some of the spherules are similar to those observed for Fe-Ni alloys containing C. They also noted that the spherules are enriched in Ni, S and P compared to the metallic phase of the Canyon Diablo meteorite, and suggested that this was due to slight selective melting of troilite-schreibersite-rich regions of the meteorite. Finally, Blau et al. (1973) argued that high Co contents of the spherules compared to Canyon Diablo metal was the result of oxidation of the spherules, enhancing the Ni and Co contents through loss of Fe oxide. This process also led to some oxidative loss of S and P (Blau et al., 1973).

In contrast, Kelly et al. (1974) noted that the S content of the spherules – 9 to 28 mg/g (Blau et al., 1973) – is not enhanced relative to an estimate of the bulk meteorite S content of 22 mg/g. This, coupled with Ni/Co and Ni/Cu ratios like those of the bulk meteorite led Kelly et al. (1974) to conclude that the spherules were formed by melting bulk Canyon Diablo material, not selective melting of troilite-schreibersite-rich regions. Kelly et al. (1974) explained the high Ni, Co and Cu contents relative to bulk meteorite by oxidation and removal of Fe.

A more recent estimate of the bulk meteorite S content is ~9-10 mg/g (Buchwald, 1975, p. 392), about half that estimated by Kelly et al. (1974) based on older modal data. Thus the S content of the spherules may be enhanced by up to a factor of ~3 compared to the bulk meteorite. Buchwald (1975, p. 392) also estimates a bulk meteorite P content of 2.5 mg/g. The spherules contain 7-14 mg/g (Blau et al., 1973), suggesting they may have up to ~6 times the P content of the bulk meteorite. This seems to support the contention of Blau et al. (1973) that some selective melting of troilite-schreibersite-rich regions occurred. However, Blau et al. (1973) did their analyses by electron microprobe using an “integrated line scan technique” on heterogeneous

samples. True bulk spherule S and P contents need to be determined to evaluate whether selective melting of troilite-schreibersite-rich regions occurred.

Figure 10 shows our INAA data on metallic spherules, along with data from Xue et al. (1995). Most spherules form a trend away from bulk Canyon Diablo towards higher Ni but lower Fe, consistent with simple loss of Fe (arrow, upper panel). A few spherules plot below the Fe-loss line. There could be two explanations for this: (i) the samples contained some iron oxides or hydrous oxides that were not removed prior to analysis, or (ii) the spherules are richer in C, P and/or S than bulk Canyon Diablo. Note that the oxide-shell samples analyzed by Xue et al. (1995) plot at a lower normalized Fe abundance than "ideal" limonite, calculated here as $FeO{\bullet}OH{\bullet}2.1H_2O$, and with higher Fe/Ni than the metal spherules they were taken from (tie lines). This is consistent with enrichment in Fe relative to the metallic core coupled with dilution by a component such as H, O, C, P and/or S. Because the oxide shells have lower bulk Fe than "ideal" limonite, some dilution by C, P and/or S must have occurred.

Cobalt-Ni, Ir-Ni and Au-Ni are well correlated in the spherules (Fig. 10). Kelly et al. (1974) argued that the Co/Ni ratios of the spherules were identical to the bulk metal of Canyon Diablo, and thus slight selective melting of troilite-schreibersite-rich regions did not occur. We find subtle variations in siderophile-element/Ni ratios in the spherules. The Co-Ni trend has a slightly lower slope than the Canyon Diablo ratio, while Au/Ni has a slightly higher slope. Regression lines pass through the mean Canyon Diablo composition (Fig. 10). This is consistent with the oxidation model of Kelly et al. (1974). Cobalt is more oxidizable than Ni. Those spherules with the highest Ni, hence having suffered the most oxidation and loss of Fe, also have Co/Ni ratios lower than bulk Canyon Diablo. Gold is less oxidizable than Ni and shows the opposite – high Au/Ni for the most Ni-rich spherules.

Four spherules have Ni contents lower than bulk Canyon Diablo. They also have the lowest sums of Fe, Co and Ni (Table 5), indicating that they contain larger amounts of diluents than do other spherules. Finally, they have high Co/Ni and low Au/Ni ratios (Fig. 10). All of these characteristics are consistent with their containing a substantial amount of the Fe- rich, Ni-Au-poor oxides produced during spherule formation. One would expect the oxide to form on the outer surface of the spherule. Thus, should these four spherules be enriched in oxides, the Co-Ni-Ir-Au-rich metallic core of the spherule somehow would have been lost during the formation process.

All of the spherules have As/Ni ratios in excess of the Canyon Diablo ratio (Fig. 10), contrary to expectations from an oxidation model. Arsenic is more easily oxidized than Ni and should be depleted relative to it, but Ni-rich spherules have As/Ni ratios of 1.89-2.79 times Canyon Diablo. The As-Ni data also scatter considerably compared to the very linear Co-Ni array (Fig. 10). Our As-Ni data closely mimic the P-Ni data of Blau et al. (1973) (Fig. 10), suggesting that the anomalous enrichment of As may be a result of slight selective melting of schreibersite-troilite-rich regions of the impactor. Arsenic and P are incompatible elements during crystallization of molten Fe-Ni, and thus will be correlated in irons (e.g., Scott, 1972). We did not find data on the As content of schreibersite, but As is in the same chemical group as P, suggesting that schreibersite exsolved from the metal may be enriched in As. Thus, the high As contents of the spherules may support slight selective melting of troilite-schreibersite-rich regions of Canyon Diablo as part of the explanation for the element enrichments.

Canyon Diablo contains troilite-graphite inclusions that are typically rimmed by schreibersite and cohenite (Buchwald, 1975). These inclusions have lower mean density than the surrounding metal. Because of this, a passing shock front will reverberate (e.g., Kieffer,

1971), and result in localized stress and temperature concentrations along metal-inclusion margins (e.g., Melosh, 1989; Stöffler et al., 1991) that will lead to enhanced localized melting at metal-inclusion interfaces. Hydrocode simulations of the Meteor Crater impact show that this will occur along the trailing edge of the impactor at moderate depths below the surface (Schnabel et al., 1999).

We conclude that both selective melting of troilite-graphite inclusions and oxidation and removal of Fe (and other elements) played roles in producing the chemical characteristics of the metallic spherules. Note that Kelly et al. (1974) and we ground off the oxide coating on the spherules before analysis. This was done under the assumption that these coating represented low-temperature rusting of the spherules. In retrospect, this most likely biased the data. The oxide coatings could well represent original high-temperature oxides produced as the spherules were airborne immediately after the impact. By grinding these off, we artificially increased the concentrations of the less oxidized elements that were concentrated in the metallic cores. True bulk analyses of spherules, including the oxide coatings, plus analyses of the different phases in Canyon Diablo are needed to evaluate the origin of the metallic spherules.

Geochemical constraints on the impact process

We have shown that the impact-melt particles contain material from the upper part of the target stratigraphy, that all are consistent with mixtures of Moenkopi and Kaibab rocks, and that those particles that seem to have been derived from lower portions of the melt zone contain less projectile material. These observations allow us to constrain the mechanism of impact melting.

One mechanism for producing dispersed impact-melts is through jetting, a process that occurs when a hypervelocity projectile meets the target at an oblique angle (see Kieffer, 1977;

Melosh, 1989). In the case of Meteor Crater, this geometry could have been satisfied when an approximately spherical Canyon Diablo meteoroid contacted the target surface, or when irregularities on the meteoroid or target surfaces meet (Fig. 11). Jetting occurs from the moment of impact until the projectile has penetrated about halfway into the target (Melosh, 1989). Roddy (1978) calculated the kinetic energy required for formation of Meteor Crater, and from this the projectile size for various assumed impact velocities. The lowest velocity used, 15 km/sec, results in a projectile about 16 m in radius, which sets the approximate maximum depth for jetting. We previously favored a shallow zone of melting for formation of some of the impact-melt glasses, <30 m (Hörz et al., 2002). This is compatible with jetting as the mechanism for formation of these melts. However, none of the impact-melt particles (this study) or the clear glasses (Hörz et al., 2002) contains only Moenkopi plus projectile components. The Moenkopi is estimated to have averaged about 8.5 m thick in the pre-impact target zone (Roddy, 1978), and thus we would expect that some impact-melts would be free of Kaibab material if jetting was the major formation mechanism. Because of this, we do not see a clear role for jetting in the production of impact-melts at Meteor Crater. Note however, that the bulk particles we have studied are mostly large, roughly cm-sized (Appendix 2), and that we found relative few clear, unaltered glasses in the samples we studied petrographically (Hörz et al., 2002). If jetting predominantly produced finer impact-melt spray, our studies could have missed those particles composed only of Moenkopi plus projectile. Thus although we find no clear signature for jetting, neither can we rule it out.

Another mechanism for formation of ballistically dispersed impact-melt particles is along the contact between the deforming projectile and the transient crater floor (Fig. 11). In this case, melting may extend to depths a few times the projectile radius (e.g., Melosh, 1989). The impact-

melts produced by this mechanism would flow up the transient crater wall and potentially mix with a range of target material during this flow. Thus, melts formed after the deformed projectile was entirely below the original target surface would have the projectile component diluted by inclusion of additional target material, including clasts. To some extent, this is compatible with our data on bulk particles. Those particles with the lowest normalized Ir content (lowest projectile component) have the strongest Kaibab signature, suggesting formation deeper in the transient crater.

Because the melt-mixing process is so chaotic, clear signatures are not preserved in the impact-melt particles. We believe our data are compatible with both jetting and melting at the transient crater-deforming projectile interface as being important in the formation of the ballistically dispersed impact-melt particles at Meteor Crater.

CONCLUSIONS

Ballistically dispersed impact-melt particles from Meteor Crater are dominantly composed of three components: the Canyon Diablo projectile, and target-rock from the Moenkopi and Kaibab formations. The compositions of the impact-melt particles do not require that rocks from the lower portions of the target section – the Toroweap and Coconino – be mixed in the melts. Although the data do not rule out up to 10% contribution from these rocks, the compositions of the impact-melt particles indicate formation only in the upper portion of the section, above these sandstones.

The impact-melt particles contain substantial projectile material. Our best estimate is that bulk particles contain on average ~14% Canyon Diablo iron, with a maximum of 20-22%. This is higher than we previously found for ballistically dispersed impact-melts from the much

smaller Wabar Crater (Mittlefehldt et al., 1992). The siderophile-element ratios are essentially unchanged from those of Canyon Diablo iron, except for Au. Many samples have Au/Ni and Au/Ir ratios much lower than for the projectile. The lowest ratios are found for impact-melt particles with the highest Kaibab component. The Br contents of Kaibab rocks are higher than those for other rocks in the section, and we suggest that fractionation of volatile Au halides may be the cause of the Au fractionation.

Metallic spherules are generally enriched in Co, Ni, Ir and Au compared to Canyon Diablo metal. Element/Ni ratios show subtle deviations from Canyon Diablo ratios that are inversely correlated with oxidizability of the element relative to Ni. We attribute this to partial oxidation of molten metal spherules during flight. Because we ground off oxide coatings from the spherules prior to analysis, our data are biased in favor of the metallic cores. The spherule compositions are consistent with slight selective melting of schreibersite-troilite-rich regions of the projectile, and this can be explained by enhanced shock melting of lower density troilite-graphite-schreibersite inclusions present in Canyon Diablo.

ACKNOWLEDGMENTS

We thank The Barringer Crater Company for permission to do field work in Meteor Crater, and the late D.J. Roddy for guiding our field collection. The senior author thanks J.H. Jones and A.H. Treiman for accompanying him in the field. We thank C.B. Moore and the Center for Meteorite Studies, ASU, for providing the impact-melt particles and metallic spherules studied here. The NASA Cosmochemistry Program supported DWM, and the Planetary Geology and Geophysics Program supported FH in these studies.

APPENDIX 1. TARGET ROCKS

Sample K-1, K-2 and C-1 through C-4 (Table 2) are small hand samples of Kaibab and Coconino that had been collect by Hörz many years ago as representative samples of these formations. Their collection locations are undocumented. Samples labeled Ma, Ka, Ta, Ca etc. are from a systematic stratigraphic section collected by Hörz and See specifically for this study. Details on these samples are given in See et al. (2002). The remaining samples described below were collected by Mittlefehldt from the crater and its vicinity.

MC-01: Moenkopi. Light pink, massive sandstone collected from the north crater wall, ~2-2.5 m above the contact with the Kaibab.

MC-02: Coconino. White, somewhat frothy and powdery sandstone fallback deposit collected from the shaft dump on the crater floor.

MC-03: Coconino. Shattered gray sandstone collected from the southwest crater wall ~70 m below the Kaibab.

MC-04: Coconino. Gray matrix of shattered sandstone collected ~10 m above sample MC-03.

MC-05: Coconino. Gray sandstone collected from the southwest crater wall ~5 m below the Kaibab.

MC-06: Kaibab. Shattered gray dolomite collected from the southwest crater wall ~15 m above the base.

MC-07: Moenkopi. Reddish siltstone/clay-rich facies collected from block in talus, southwest crater wall.

MC-08: Toroweap. Gray sandstone collected from the overturned flap on the southwest crater rim.

MC-09: Coconino. Highly shocked ejecta debris collected from south crater rim.

MC-10: Kaibab. Gray dolomite collected from overturned flap on the west crater rim.

MC-11: Coconino. Gray sandstone collected from stream cut, Oak Creek Canyon.

MC-12: Kaibab. Gray dolomite collected from boulder float in stream cut, Oak Creek Canyon.

MC-13: Toroweap. Knobby gray sandstone collected from the overturned flap on the southwest crater rim.

APPENDIX 2. IMPACT-MELT PARTICLES

H11: This is a composite of 15 individual irregularly shaped cm-sized impact-melt particles. The particles are vesicular with dark gray interiors, and thin brownish rims. The particles were individually ground, and the powders mixed and homogenized to produce a bulk sample with a total mass of about 4 grams.

H11a: This is an individual cm-sized irregularly shaped impact-melt particle from the same group used to prepare H11. This particle was much harder to grind than the others, and was kept separate for that reason.

IIG-1: This is an irregularly shaped dark brown vesicular impact-melt particle ~1.8x1.3x1.3 cm in size. Vesicles are up to ~4 mm in size. Numerous small clasts are present. Some secondary minerals are present both on the surface and in interior vesicles. Two samples (IIG-1a and IIG-1b) were hand-picked from the freshest material.

IIG-2: This is an irregularly shaped dark brown impact-melt particle ~1.8x1.4x1.4 cm in size containing very few vesicles, generally ~1-2 mm in size. Numerous small clasts are present. Some secondary minerals are present both on the surface and in interior vesicles. Two samples (IIG-2a and IIG-2b) were hand-picked from the freshest material.

IIG-3: This is an irregularly shaped dark brown impact-melt particle ~1.9x1.1x1.1 cm in size containing few vesicles generally ~1 mm or less in size. Little clastic material is present. Some secondary minerals occur both on the surface and in interior vesicles. Four samples (IIG-3a through IIG-3d) were hand-picked from the freshest material.

IIG-4: This is a smooth, but highly irregularly shaped impact-melt particle. The particle is composed of black to red-black glass and yellow-brown material that appears to be melted clastic debris. The interior is cored with this melted clastic material. A fairly

pure impact-glass sample (IIG-4) and a fairly pure clast sample (IIG-4c) were hand-picked.

M1: Large (7 mm) accretionary sphere of black glass with many accretionary promontories and splashes. Some of the latter are flattened and transitional to the dark matrix glass, giving the surface a somewhat swirly appearance. One side is rough, the other is smooth. The bead is vesicular and almost a hollow shell. Some of the interior surfaces and interior small vesicles contain fine-grained secondary minerals.

M2: Beautifully flattened, large (5x3 mm) dense black shiny spheroid with sugary surfaces on all sides. It contains no prominent accretions, but has one hemispherical depression. The bead is very magnetic, and is an oxide bead.

M3: Large (9 mm) fairly rounded bead of brownish color. Upon splitting, the interior is highly porous and appears weathered with a distinctly orange, oxidized skin. This exterior surface is dull, pitted and of sugary appearance. Some quartz clasts are present. Samples M3a and M3b are two different samples of hand-picked material.

M4: Large (8 mm) ellipsoid of dark glass with somewhat grayish hue. It appears to be a mixture of dark glass and a lighter grayish glass. Many accretionary particles are present on all sides. The interior is vesicular and nearly hollow, and contains secondary minerals. There is a patch of fine-grained, white sugary material that may be a glassy clast. Sample M4a is hand-picked glassy material, while M4b is hand-picked material enriched in secondary minerals.

M5: Stubby ellipsoid (4 mm), possibly stubby cylinder of dark colored, fresh-appearing glass. The surface is dull and sugary with many small holes or pits. The interior is very porous,

essentially frothy. Accretionary features are abundant and display a bi-modal distribution. Interior vesicles contain some secondary minerals.

M6: Large (12 mm), broken, ropy and cylindrical lapillus of dull glass with a pitted surface. There are many accretionary particles on the surface, and a few clasts are present. A fresh fracture surface displays two types of material; a dark, very porous glass matrix and tan inclusions, either of melt or finely crystalline material (weathered?).

M7: Exceptionally nice, round sphere (3 mm) of dark glass with numerous accretionary beads. A modestly lighter colored glass makes distinct promontories and knobs. The interior is very porous at microscopic scales. There are some clasts in the interior, and a small amount of fine-grained secondary minerals.

M8: A classic "impactite" of Nininger: highly porous, slag-like, weathered glass of brown color containing numerous pockets of clasts and distinctly different colored melts. The rim is modestly oxidized. This sample was very friable. Sample M8a is hand-picked coarse fragments from the sample crushing, while M8b is the fine debris produced during crushing.

M10: A typical dull, dark colored impactite. It is coarsely porous and somewhat weathered with an oxidized rim, but only a small amount of fine-grained secondary minerals.

M11: A large (12-15 mm) flattened ellipsoid of porous, tan melt. The surface is unusually sculptured with polygons forming an almost cauliflower-like texture. Some of the polygons are of dark melt, but the majority is light-tan in color. The sample is highly altered.

M12: An impact-melt particle of unusually fresh, tektite-like, dense glass of black color, almost volcanic in appearance. The sample is very fresh, and clast-poor; possibly clast-free.

M13: A very large (14 mm) typical impactite of rusty-brown colored glass. The surface is dull and sugary in appearance with no good accretionary features but is definitely an aerodynamically shaped particle. The interior is frothy and has a red colored weathering rind surrounding a dark gray/black core. Sample M13a is reddish rind glass, while M13b is black interior glass.

M14: A large (8 mm long) elongated, ropy lapillus fragment. The surface has numerous weathered knobs of dull, dust-covered secondary material and some clasts. There are two types of glass; dark glass and honey-yellow glass. The interior is frothy, with little clastic material.

M15: A large, ropy lapillus fragment (about 15 mm long) with many accretionary surface features mostly of dark glass. Some patches of secondary minerals are present on the surface. The interior shows yellowish weathering rind glass with a fresh black glass core. Some clastic material is present in the particle. The sample was very tough to break.

M16: A distinctly rusty-colored, highly porous aerodynamically shaped melt object. It does not have distinct dense skin; most of the particle is altered, with only a little fresh, dark gray to black glass in the interior. It contains some clastic material (quartz).

M17: A large (11 mm) ropy, elongate lapillus of dense dark melt with many accretionary knobs on the surface. The interior includes fresh black glass plus reddish, altered glass.

M18: A large ovoid lapillus (16 mm) with a grayish-white surface due to partial coating by secondary minerals, and bleaching of the underlying glass. Numerous honey-colored pockets are visible. The fresh fracture surface reveals intimate mixing of the different colored glasses, but the particle contains a distinct, bleached rind. Sample M18a is hand-

picked interior glass, but containing some bleached glass; M18b is enriched in the bleached glass; M18c is exterior material enriched in secondary minerals.

M19: A flat, pancake shaped object displaying prominent ridges showing material flow and aerodynamic shaping. The interior is porous, somewhat weathered black glass with a distinctly rusty-colored, orange oxidation rim. Some secondary minerals are present on the exterior.

M20: A small irregular fragment of dense mostly honey-colored glass. Part of the exterior surface is preserved and the fragment was clearly derived from some sort of ballistic bead.

M21: A very fresh appearing bead of yellow glass with knobs and accretionary promontories of both black and yellow glasses, i.e. a mixed melt. No secondary minerals are present.

M22: This sample is a hollow hemisphere – a fragment of a hollow sphere - with a smooth outer surface. The interior glass is dark and contains numerous microvesicles.

M23: An elongate bead of yellow glass with prominent accretionary knobs. Some black glass is present in the interior.

M24: A large (9 x 2 mm) dumbbell of relatively dense, dark glass, somewhat sugary, and with a pitted surface. A very thin weathering rind is present.

M25: A fresh, small (3-4 mm) bead of dark glass with a distinctly shiny surface. The distribution of accretionary features is uneven. The interior contains some vesicles, and a few clasts.

M26: This is a cylindrical object of unusual dark wine-red color. The particle is fairly fresh with shiny surfaces and no prominent accretionary features. The interior contains some black glass.

M27: This is a very fresh sphere of dense dark glass with a smooth, shiny surface. The interior is composed of fresh dark frothy glass, with a thin alteration rind.

SIG-1: This is an oblong hollow spheroid ~5x4x4 mm in size with a few protuberances. One end contains many <1 mm size vesicles. The interior cavity is filled with secondary minerals. Several fresh, black glass fragments were hand-picked for analysis.

SIG-2: This is an almost perfect hollow sphere ~4 mm in size with a few protuberances and many <0.5 mm size vesicles. This sample contained relatively little secondary material. One piece of fresh glass was hand-picked for analysis.

SIG-3: This is a flattened (on one side) spheroid ~5 mm in size with a large protuberance on the flattened side. There are a few <1 mm size vesicles. This sample was partially hollow – a clast occupies part of the center. Several fragments of impact glass were selected for analysis (SIG-3) and a sample of secondary minerals was selected (SIG-3w).

SIG-4: This is a slightly vesicular smooth brown glass hollow ball. There is a red-brown weathering rind surrounding fresh black glass. The interior cavity is small, and partially filled with white secondary minerals.

APPENDIX 3. INAA DATA ON MISCELLANEOUS SAMPLES

TABLE A1. COMPOSITIONS OF MISCELLANEOUS SAMPLES FROM METEOR CRATER DETERMINED BY INAA*.

		IIG-4c clast‡		SIG-3w sec min‡		M4b sec min‡		M18c sec min‡		M2 oxide‡	
mass†	mg	16.73	±	3.99	±	1.05	±	20.91	±	54.58	±
Na	µg/g	324	4	1800	20	169	4	1010	10	12.6	0.8
K_2O	wt%	0.91	0.02	1.25	0.03			0.28	0.01	0.014	0.007
CaO	wt%	18	1	3.9	0.5	50	2	17.4	0.6		
Sc	µg/g	4.05	0.05	4.25	0.05	0.12	0.01	2.11	0.02	0.11	0.03
Cr	µg/g	46	1	34	2			56.7	0.9	15	1
Fe	mg/g	54.6	0.6	13.2	0.4	2.1	0.2	56.5	0.6	712	7
Co	µg/g	213	2	18.0	0.2	15.6	0.3	254	3	2730	30
Ni	mg/g	3.27	0.08	0.11	0.02	0.2	0.1	3.53	0.07	14.1	0.3
Zn	µg/g							23	3		
As	µg/g	3.15	0.08	3.0	0.2	2.6	0.3	3.3	0.1	0.9	0.2
Br	µg/g	0.48	0.05	1.3	0.2	28	1	2.4	0.1		
Rb	µg/g	28	4	42	5			11	2		
Sr	µg/g			120	60			350	20		
Zr	µg/g	260	40	450	60			240	30		
Sb	ng/g	220	20	480	40			210	10		
Cs	µg/g	2.39	0.06	2.76	0.08			0.85	0.03		
Ba	µg/g	690	20	310	30	1000	200	3440	80		
La	µg/g	14.2	0.2	16.6	0.2	4.4	0.1	7.77	0.09	0.35	0.01
Ce	µg/g	28.0	0.5	29.6	0.8			16.2	0.3		
Nd	µg/g	12	3					9	3		
Sm	µg/g	3.04	0.04	2.72	0.04	0.51	0.03	1.62	0.02	0.053	0.005
Eu	µg/g	0.65	0.02	0.54	0.02			0.377	0.009		
Tb	µg/g	0.42	0.03	0.38	0.04			0.24	0.01		
Yb	µg/g	1.60	0.04	1.49	0.08			0.94	0.03		
Lu	µg/g	0.245	0.008	0.22	0.02	0.10	0.05	0.145	0.008		
Hf	µg/g	7.5	0.2	12.2	0.3			7.0	0.1		
Ta	ng/g	480	40	470	40			300	20		
W	ng/g	380	80	1100	300					700	300
Ir	ng/g	38	3					92	2		
Au	ng/g	4.7	0.7			24	9	10.9	0.9	33	2
Th	µg/g	4.0	0.1	4.3	0.2			2.10	0.06		
U	µg/g	1.56	0.06	1.4	0.1			1.52	0.06		

*Note in this table Ni is given in units of mg/g. Individual uncertainties given in the ± columns.
†mass refers to mass in mg of analyzed material and represents most or all of the mass of sample prepared.
‡clast - lithic clast separated from impact melt particle IIG-4; sec min - secondary minerals found in impact melt particles SIG-3, M4 and M18; oxide - rounded oxide bead.

REFERENCES CITED

Attrep, M. Jr., Orth, C.J., Quintana, L.R., Shoemaker, C.S., Shoemaker, E.M. and Taylor, S.R., 1991, Chemical fractionation of siderophile elements in impactites from Australian meteorite craters [abs.]: Lunar and Planetary Science v. XXII, p. 39-40.

Benedix, G.K., McCoy, T.J., Keil, K. and Love, S.G., 2000, A petrologic study of the IAB iron meteorites: Constraints on the formation of the IAB-Winonaite parent body: Meteoritics and Planetary Science v. 35, p. 1127-1141.

Blau, P.J., Axon, H.J. and Goldstein, J.I., 1973, Investigation of the Canyon Diablo metallic spheroids and their relationship to the breakup of the Canyon Diablo meteorite: Journal of Geophysical Research v. 78, p. 363-374.

Boyd, F.R. and Mertzman, S.A., 1987, Composition and structure of the Kaapvaal lithosphere, southern Africa, in Mysen, B.O., ed., Magmatic Processes: Physicochemical Principles: University Park, Pennsylvania, Geochemical Society, p. 13-24.

Brett, R., 1967, Metallic spherules in impactite and tektite glasses: American Mineralogist v. 52, p. 721-733.

Brown, R.W., 1977, A sample fusion technique for whole rock analysis with the electron microprobe: Geochimica et Cosmochimica Acta v. 41, p. 435-438.

Buchwald, V.F., 1975, Handbook of Iron Meteorites: Berkeley, University of California Press, 1418 p.

Bunch, T.E., Keil, K. and Olsen, E., 1970, Mineralogy and petrology of silicate inclusions in iron meteorites: Contributions to Mineralogy and Petrology v. 25, p. 297-340.

Choi, B.-G., Ouyang, X. and Wasson, J.T., 1995, Classification and origin of IAB and IIICD iron meteorites: Geochimica et Cosmochimica Acta v. 59, p. 593-612.

Dence, M.R., 1971, Impact melts: Journal of Geophysical Research v. 76, 5552-5556.

Gibbons, R.V., Hörz, F., Thompson, T.D. and Brownlee, D.E., 1976, Metal spherules in Wabar, Monturaqui, and Henbury impactites, in Proceedings, Lunar Science Conference, 7th, New York: New York, Pergamon Press, p. 863-880.

Grieve, R.A.F., 1982, The record of impact on Earth: Implications for a major Cretaceous/Tertiary impact event, in Silver, L.T., and Schultz, P.H., eds., Geological implications of impacts of large asteroids and comets on the earth: Geological Society of America Special Paper 190, p. 25-37.

Grieve, R.A.F., 1991, Terrestrial impact: The record in the rocks: Meteoritics v. 26, p. 175-194.

Hagerty, J.J. and Newsom, H.E., 2003, Hydrothermal alteration at the Lonar Lake impact structure, India: Implications for impact cratering on Mars: Meteoritics and Planetary Science v. 38, p. 365-381.

Hörz, F., See, T.H., Murali, A.V. and Blanchard, D.P., 1989, Heterogeneous dissemination of projectile materials in the impact melts from Wabar crater, Saudi Arabia, in Proceedings,

Lunar and Planetary Science Conference, 19th, Houston: Texas, Lunar and Planetary Institute, p. 697-709.

Hörz, F., Mittlefehldt, D.W., See, T.H. and Galindo, C., 2002, Petrographic studies of the impact melts from Meteor Crater, Arizona, USA: Meteoritics and Planetary Science v. 37, p. 501-531.

Kargel, J.S., Coffin, P., Kraft, M., Lewis, J.S., Moore, C., Roddy, D., Shoemaker, E.M. and Wittke, J.H., 1996, Systematic collection and analysis of meteoritic materials from Meteor Crater, Arizona [abs.]: Lunar and Planetary Science v. XXVII, p. 645-646.

Kelly, W.R., Holdsworth, E. and Moore, C.B., 1974, The chemical composition of metallic spheroids and metallic particles within impactite from Barringer Meteorite Crater, Arizona: Geochimica et Cosmochimica Acta v. 38, p. 533-543.

Kieffer, S.W., 1971, Shock metamorphism of the Coconino Sandstone at Meteor Crater, Arizona: Journal of Geophysical Research v. 76, p. 5449-5473.

Kieffer, S.W., 1977, Impact conditions for formation of melt by jetting in silicates, in Roddy, D.J., Pepin, R.O., and Merrill, R.B., eds., Impact and Explosion Cratering: New York, New York, Pergamon Press, p. 751-769.

King, D.T. Jr., Neathery, T.L., Petruny, L.W., Koeberl, C. and Hames, W.E., 2002, Shallow-marine impact origin of the Wetumpka structure (Alabama, USA): Earth and Planetary Science Letters v. 202, p. 541-549.

Lide, D.R., ed., 2001, CRC Handbook of Chemistry and Physics, 82nd Edition, CRC Press, Boca Raton, FL.

Melosh, H.J., 1989, Impact Cratering A Geologic Process. Oxford Univ. Press, New York, 245 pp.

Mittlefehldt, D.W. and Lindstrom, M.M., 1991, Generation of abnormal trace element abundances in Antarctic eucrites by weathering processes: Geochimica et Cosmochimica Acta v. 55, p. 77-87.

Mittlefehldt, D.W. and Lindstrom, M.M., 1993, Geochemistry and petrology of a suite of ten Yamato HED meteorites, in Proceedings, National Institute of Polar Research Symposium on Antarctic Meteorites 17th, no. 6, p. 268-292.

Mittlefehldt, D.W., See, T.H. and Hörz, F., 1992, Dissemination and fractionation of projectile materials in the impact melts from Wabar Crater, Saudi Arabia: Meteoritics v. 27, p. 361-370.

Mittlefehldt, D.W., McCoy, T.J., Goodrich, C.A. and Kracher, A., 1998, Non-chondritic meteorites from asteroidal bodies, in Papike, J.J., ed., Planetary Materials, Reviews in Mineralogy, v. 36, p. 4-1 – 4-195.

Mittlefehldt, D.W. Hörz, F. and See, T.H., 2000, Trace element chemistry of Meteor Crater impact-melt particles and target rocks - Empirical evidence on the cratering process [abs.]: Lunar and Planetary Science v. XXXI, #1798.

Morgan, J.W., Higuchi, H., Ganapathy, R. and Anders, E., 1975, Meteoritic material in four terrestrial meteorite craters, in Proceedings, Lunar Science Conference, 6th, New York: New York, Pergamon Press, p. 1609-1623.

Nininger, H.H., 1956, Arizona's Meteorite Crater. World Press, Denver, CO, 232 pp.

Nishiizumi, K., Kohl, C.P., Shoemaker, E.M., Arnold, J.R., Klein, J., Fink, D. and Middleton, R., 1991, In situ ^{10}Be-^{26}Al exposure ages at Meteor Crater, Arizona: Geochimica et Cosmochimica Acta v. 55, p. 2699-2703.

Palme, H., Janssens, M.-J., Takahashi, H., Anders, E. and Hertogen, J., 1978, Meteoritic material at five large impact craters: Geochimica et Cosmochimica Acta v. 42, p. 313-323.

Phillips, F.M., Zreda, M.G., Smith, S.S., Elmore, D., Kubik, P.W., Dorn, R.I. and Roddy, D.J., 1991, Age and geomorphic history of Meteor Crater, Arizona, from cosmogenic ^{36}Cl and ^{14}C in rock varnish: Geochimica et Cosmochimica Acta v. 55, p. 2695-2698.

Roddy, D.J., 1978, Pre-impact geologic conditions, physical properties, energy calculations, meteorite and initial crater dimentions and orientations of joints, faults and walls at Meteor Crater, Arizona, in Proceedings, Lunar and Planetary Science Conference, 9th, New York: New York, Pergamon Press, p. 3891-3930.

Roddy, D.J., Boyce, J.M., Colton, G.W. and Dial, A.L. Jr., 1975, Meteor Crater, Arizona, rim drilling with thickness, structural uplift, diameter, depth, volume, and mass-balance calculations, in Proceedings, Lunar Science Conference, 6th, New York: New York, Pergamon Press, p. 2621-2644.

Schnabel, C., Pierazzo, E., Xue, S., Herzog, G.F., Masarik, J., Cresswell, R.G., di Tada, M.L., Liu, K. and Fifield, L.K., 1999, Shock melting of the Canyon Diablo impactor: Constraints from Nickel-59 contents and numerical modeling: Science v. 285, p. 85-88.

Scott, E.R.D., 1972, Chemical fractionation in iron meteorites and its interpretation: Geochimica et Cosmochimica Acta v. 36, p. 1205-1236.

Scott, E.R.D. and Wasson, J.T., 1975, Classification and properties of iron meteorites: Reviews of Geophysics and Space Physics v. 13, p. 527-546.

Scott, E.R.D., Haack, H. and McCoy, T.J., 1996, Core crystallization and silicate-metal mixing in the parent body of the IVA iron and stony-iron meteorites: Geochimica et Cosmochimica Acta v. 60, p. 1615-1631.

See, T.H., Hörz, F., Mittlefehldt, D.W., Varley, L., Mertzman, S. and Roddy, D., 2002, Major element analyses of the target rocks at Meteor Crater, Arizona. NASA/TM-2002-210787, 23 p.

Shoemaker, E.M., 1963, Impact mechanics at Meteor Crater, Arizona, in Middlehurst, B.M., and Kuiper, G.P., eds., The Moon, Meteorites, and Comets: Chicago, Illinois, University of Chicago Press, p. 301-336.

Shoemaker, E.M., 1987, Meteor Crater, Arizona, in Beus, S.S., ed., Rocky Mountain Section of the Geological Society of America Centennial Field Guide: Boulder, Colorado, Geological Society of American, v. 2, p. 399-404.

Simonds, C.H., Floran, R.J., McGee, P.E., Phinney, W. C. and Warner, J.L., 1978, Petrogenesis of melt rocks, Maicouagan, impact structure, Quebec: Journal of Geophysical Research v. 83, p. 2773-2788.

Stöffler, D., Keil, K. and Scott, E.R.D., 1991, Shock metamorphism of ordinary chondrites: Geochimica et Cosmochimica Acta v. 55, p. 3845-3867.

Wasson, J.T. and Kimberlin, J., 1967, The chemical classification of iron meteorites, II: Irons and pallasites with germanium concentrations between 8 and 100 ppm: Geochimica et Cosmochimica Acta v. 31, p. 2065-2093.

Wasson, J.T. and Ouyang, X., 1990, Compositional range in the Canyon Diablo meteoroid: Geochimica et Cosmochimica Acta v. 54, p. 3175-3183.

Wasson, J.T. and Richardson, J.W., 2001, Fractionation trends among IVA meteorites: Contrasts with IIIAB trends: Geochimica et Cosmochimica Acta v. 65, p. 951-970.

Xue, S., Herzog, G.F., Hall, G.S., Klein, J., Middleton, R. and Juenemann, D., 1995, Stable nickel isotopes and cosmogenic beryllium-10 and aluminum-26 in metallic spheroids from Meteor Crater, Arizona: Meteoritics v. 30, p. 303-310.

TABLE 1. MAJOR-ELEMENT COMPOSITIONS OF TARGET ROCKS AND A COMPOSITE OF SEVERAL IMPACT-MELT PARTICLES DETERMINED BY XRF AND IRON TITRATION.*

	Moenkopi		Kaibab					Toroweap
	MC-01	MC-07	K-1	K-2	MC-06	MC-10	MC-12	MC-08
SiO_2	83.94	57.76	14.52	2.41	45.36	35.31	44.12	95.74
TiO_2	0.44	0.49	0.04	0.01	0.12	0.10	0.09	0.08
Al_2O_3	6.95	6.14	0.78	0.13	2.09	2.28	1.48	1.62
Fe_2O_3	0.86	1.58	0.11	0.28	0.19	0.16	0.70	0.00
FeO	0.34	0.14	0.07	0.20	0.07	0.16	0.06	0.11
MnO	0.03	0.06	0.02	0.03	0.04	0.03	0.02	0.00
MgO	0.39	1.44	18.12	20.77	10.60	12.18	10.70	0.03
CaO	2.01	16.05	26.82	30.83	15.60	19.25	16.65	0.54
Na_2O	0.02	0.04	0.07	0.07	0.07	0.06	0.07	0.00
K_2O	1.24	1.17	0.15	0.03	0.44	0.45	0.26	0.46
P_2O_5	0.13	0.13	0.03	0.03	0.17	0.45	0.46	0.03
LOI	3.72	15.23	39.19	44.43	24.88	28.93	25.11	1.31
sum	100.07	100.23	99.92	99.22	99.63	99.36	99.72	99.92

			Coconino					impact-melt
	C-3[†]	MC-02	MC-04	MC-05	MC-05	MC-09	MC-11a	H11
SiO_2	71.83	97.81	95.48	96.30	96.12	92.15	99.12	48.27
TiO_2	0.02	0.04	0.09	0.06	0.07	0.14	0.02	0.20
Al_2O_3	0.96	1.14	2.63	2.17	2.26	4.11	0.72	2.90
Fe_2O_3	0.02	0.05	0.20	0.29	0.08	0.13	0.14	7.05
FeO	0.05	0.06	0.11	0.05	0.06	0.06	0.06	16.48
MnO	0.00	0.00	0.00	0.00	0.00	0.00	0.00	0.08
MgO	0.78	0.00	0.04	0.05	0.06	0.22	0.00	8.24
CaO	14.55	0.10	0.13	0.10	0.11	0.45	0.05	12.00
Na_2O	0.00	0.00	0.00	0.00	0.01	0.00	0.00	0.09
K_2O	0.13	0.18	0.52	0.59	0.60	0.60	0.07	0.32
P_2O_5	0.13	0.02	0.03	0.03	0.03	0.04	0.02	0.44
LOI	12.01	0.53	0.96	0.75	0.75	1.77	0.37	1.40
sum	100.48	99.93	100.19	100.39	100.15	99.67	100.57	97.47

[†]This sample from an undocumented location is anomalous in CaO content, likely reflecting secondary calcite cement.

TABLE 2. COMPOSITIONS OF METEOR CRATER TARGET ROCKS DETERMINED BY INAA*.

		Moenkopi Formation							Kaibab Formation																
		Ma	Mb	Mc	Md	Me	MC-01	MC-07	Ka	Kb	Kc	Kd	Ke	Kf	Kg	Kh	Ki	Kj	Kk	Kl	MC-06	MC-10	MC-12	K-1	K-2
mass†	mg	105.33	81.18	70.64	72.05	84.83	62.99	73.91	109.88	98.15	94.31	102.02	80.19	87.40	81.43	93.46	91.30	92.20	101.52	87.05	66.05	79.30	63.85	72.87	66.84
Na	µg/g	284	358	363	355	372	322	349	229	364	300	272	295	263	270	259	236	222	249	213	478	269	246	389	222
K_2O	wt%	1.16	1.46	1.69	1.53	1.44	1.22	1.24	0.48	0.46	0.72	0.53	0.56	0.58	0.260	0.61	0.269	0.50	0.58	0.70	0.45	0.49	*0.234*	0.222	0.043
CaO	wt%	7.2	9.3	8.4	10.6	13.1	2.0	15.0	13.5	18.0	11.7	17.4	17.2	17.4	24.6	15.7	24.6	18.0	18.6	15.4	15.2	19.2	16.0	26	29
Sc	µg/g	3.98	6.54	8.02	7.29	6.51	3.84	4.87	0.96	0.91	1.17	1.07	1.01	1.23	0.604	1.63	0.89	0.772	1.41	2.38	0.722	1.08	0.96	0.625	0.159
Cr	µg/g	24.0	29.3	32.4	24.1	27.3	15.7	37.2	30.6	23.9	32.9	32.3	27.3	28.6	8.2	15.6	8.0	22.6	14.4	23.8	28.0	25.4	34.8	12.2	5.6
Fe	mg/g	6.49	15.46	19.10	20.25	17.26	8.21	13.20	2.13	2.18	1.53	3.11	2.09	2.68	2.14	2.67	3.45	3.49	4.14	11.70	1.68	2.04	4.80	1.29	3.72
Co	µg/g	7.48	5.13	5.81	10.5	8.8	2.47	4.32	3.08	2.86	1.65	1.99	1.55	1.60	0.83	0.96	1.01	1.08	2.09	15.0	1.70	1.82	2.86	1.49	2.14
Ni	µg/g					14	16		7	8	8	11	13	10	7	7	6	5	9	37	8	10	20	10	10
Zn	µg/g	33	44	58	82	59	22.2	36	19.6	21.6	18.5	19.1	16.1	18.2	24.0	24.5	27.9	22.1	26.8	64	27.8	13.0	132		
As	µg/g	7.3	3.30	4.14	6.2	4.21	1.55	3.12	1.48	1.27	1.44	6.38	2.40	1.61	2.14	4.71	1.65	3.13	9.8	22.0	9.4	*1.00*	11.4	2.16	1.91
Se	µg/g		0.4						1.2	1.4	1.1	0.88	1.3	0.9	0.10	0.22			0.14		1.0	1.49	1.3		
Br	µg/g	0.42	0.46	0.45	0.43	0.53	*0.18*	0.40	1.10	1.26	1.00	2.0	1.46	1.02	2.2	1.28	1.10	1.07	0.81	0.79	1.36	1.07	1.00	3.0	1.07
Rb	µg/g	33	48	56	46	46	38	40	13.3	12.0	19.0	14.4	14.8	16.0	7.2	16.7	8.2	14.0	16.8	20.9	12.9	13.9	6.6	*6.1*	
Sr	µg/g	74	80	82	73	93	72	88	310	89	75	108	101	149	87	107	97	109	102	101	67	97	70	110	87
Zr	µg/g	460	360	230	150	210	370	470	140	100	200	140	160	150	58	160	61	150	90	200	140	100	100	55	
Sb	ng/g	374	451	530	440	440	343	389	203	160	199	285	176	177	131	197	104	166	218	500	287	140	560	118	*40*
Cs	µg/g	1.82	5.22	5.96	3.37	4.34	1.97	3.59	0.64	0.65	0.89	0.89	0.66	0.89	0.319	0.75	0.434	0.71	1.20	1.36	0.61	0.84	0.419	0.330	*0.052*
Ba	µg/g	207	440	308	304	269	191	207	198	88	229	180	137	151	64	193	78	114	105	140	142	97	63	65	*16*
La	µg/g	9.8	16.4	17.8	14.4	16.7	11.2	19.5	4.82	3.60	4.84	4.19	4.04	6.57	2.26	4.18	2.68	5.07	5.00	7.78	4.02	4.45	8.8	2.13	0.736
Ce	µg/g	21.0	33.1	36.1	29.5	33.0	25.0	38.0	8.4	6.5	8.7	7.4	7.3	8.5	4.06	7.4	4.56	8.0	8.4	14.1	7.6	7.9	7.2	4.20	*1.33*
Nd	µg/g	11	14	17	13	16	13	21	5.1	3.0	4.9	3.7	3.7	5.1	2.2	4.2	2.9	5.2	4.7	8.4	4.1	4.6	7	*1.8*	
Sm	µg/g	2.65	3.65	3.84	3.45	3.74	2.79	4.32	1.24	0.74	0.96	0.87	0.83	1.11	0.463	0.89	0.541	0.93	0.89	1.65	0.69	0.87	1.40	0.426	0.155
Eu	µg/g	0.65	0.84	0.88	0.81	0.86	0.69	0.92	0.289	0.159	0.211	0.191	0.181	0.233	0.091	0.203	0.110	0.191	0.182	0.365	0.148	0.197	0.286	0.089	*0.029*
Tb	µg/g	0.415	0.56	0.56	0.52	0.55	0.411	0.66	0.173	0.099	0.129	0.126	0.111	0.160	0.060	0.126	0.074	0.124	0.116	0.240	0.086	0.120	0.198	0.057	*0.026*
Yb	µg/g	1.82	2.17	1.91	1.68	1.98	1.51	2.65	0.55	0.432	0.61	0.57	0.55	0.73	0.271	0.57	0.345	0.55	0.52	0.94	0.446	0.52	0.87	0.256	*0.083*
Lu	µg/g	0.292	0.336	0.294	0.253	0.303	0.235	0.420	0.090	0.071	0.103	0.096	0.090	0.118	0.040	0.090	0.055	0.088	0.081	0.146	0.077	0.085	0.130	0.043	0.027
Hf	µg/g	13.0	10.2	6.2	4.64	6.1	11.1	16.0	4.18	2.87	5.6	4.11	4.46	4.12	1.53	4.14	1.63	3.88	2.55	5.39	4.68	3.11	2.99	1.71	0.36
Ta	ng/g	580	540	500	390	500	570	690	197	144	211	167	151	163	81	137	86	138	144	254	177	167	108	68	9
W	ng/g	770	800	820	650	710	630	850	270	200	270	210	200	200	200	230	160	240	280	460	400	180	310	210	*80*
Au	ng/g			*0.6*					1.1	*0.4*	*0.6*	2.8	*0.4*	*0.5*	1.2	*0.5*	1.0	2.0	2.3		0.7	*0.6*	20.2	1.4	0.7
Th	µg/g	3.69	4.87	5.26	4.25	4.54	3.44	5.97	1.09	0.91	1.27	1.03	1.00	1.19	0.461	0.94	0.58	1.02	1.12	1.80	0.90	0.96	0.92	0.55	*0.090*
U	µg/g	1.73	1.55	1.60	1.83	1.56	1.16	2.25	3.06	2.40	2.85	2.41	2.76	2.08	2.20	1.40	1.70	1.41	1.20	1.53	3.37	2.04	4.7	1.34	1.86

*Note that in this table Ni is given in units of µg/g. Ir in all target rocks was below the 2σ detection limit of ~1 ng/g. Typical 1σ relative uncertainties are: ≤2% - Na, Sc, Fe, Co, La, Sm; 1-3% - Cr, As, Cs, Ce, Eu, Yb, Hf, Th, U; 2-5% - K_2O, CaO, Zn, Sb, Ba, Tb, Lu, Ta; 4-8% - Br, Rb; 5-10% - Se; 5-20% Sr, Au; 10-20% - Zr, Nd W; 15-50% - Ni. Values in italics have uncertainties 1.33-3× the upper end of the typical uncertainty range. Underlined values have uncertainties 3-6× the upper end of the typical uncertainty range. In all cases, the proper number of significant digits are used.

†mass refers to weight in mg of analyzed material; samples were splits of homogenized powders of much larger mass.

TABLE 2. CONTINUED.

		Toroweap Formation				Coconino Formation													
		Ta	Tb	MC-08	MC-13	Ca	Cb	Cc	Cd	MC-02	MC-03	MC-04	MC-05	MC-09	MC-11a	MC-11b	C-1	C-2	C-3‡	C-4
mass†	mg	105.98	97.53	77.33	65.78	117.32	108.48	133.77	117.47	71.98	64.39	76.93	76.07	65.33	65.16	72.15	116.90	127.84	80.82	85.3
Na	µg/g	74.1	119	49.6	154	132	90.2	55.9	60.5	39.1	62.5	31.2	37.5	126	*22.9*	*16.4*	128	73	88	27.3
K_2O	wt%	0.284	0.43	0.192	0.66	0.216	0.238	0.158	0.184	0.137	0.236	0.115	0.146	0.46	*0.085*	*0.038*	0.35	0.28	0.135	0.106
CaO	wt%	0.15	1.53	*0.30*	3.4	0.07	0.09	0.06	*0.13*					0.26					13.7	0.05
Sc	µg/g	0.514	1.18	0.393	0.775	0.714	1.05	0.490	0.479	0.496	1.03	0.479	0.353	1.27	0.421	0.222	1.25	0.639	0.369	0.342
Cr	µg/g	17.6	18.5	12.6	36.4	9.4	18.2	11.0	12.7	4.3	7.6	4.0	7.9	14.3	*2.6*	*1.7*	11.9	7.6	9.2	*3.0*
Fe	mg/g	0.892	1.017	0.378	0.696	0.530	0.570	0.363	0.438	0.338	0.527	0.357	0.284	0.830	1.524	0.469	0.581	0.427	0.277	0.257
Co	µg/g	0.83	0.70	0.187	0.427	1.25	0.426	0.239	0.203	0.166	0.265	0.104	0.118	0.61	0.328	0.311	4.31	0.389	0.64	0.157
Ni	µg/g	4							2										9	
Zn	µg/g	7.3	9.9	2.5	5.5	7.2	5.7	2.9	3.6	3.4	4.5	2.2	2.2	10.4	12.3	5.1				
As	µg/g	5.84	2.55	*0.59*	1.65	0.69	1.12	0.42	1.17	0.57	1.51	0.78	0.79	2.01	5.7	2.11	1.42	0.77	1.06	0.49
Se	µg/g		0.14												0.95	0.44			0.15	
Br	µg/g	0.40	0.46	0.36	0.62	0.32	0.38	0.29	0.35	0.23	0.20	0.22	0.27	0.38	0.28	0.28	0.44	0.31	1.91	0.34
Rb	µg/g	8.0	11.8	5.2	19.3	6.2	7.0	4.5	5.3	4.0	7.0	3.9	3.6	12.9	2.5	*1.3*	10.1	7.7	3.4	3.4
Sr	µg/g	137	188	*8*	600	29	38	28	38	25	33	16	36	48	11	*8*	43	23	90	23
Zr	µg/g	73	130	150	150	110	120	43	70	40	120	48	32	120	21	21	100	16	28	17
Sb	ng/g	186	170	155	196	72	99	76	102	67	95	64	74	1000	104	63	119	82	68	64
Cs	µg/g	0.417	0.57	0.276	1.02	0.270	0.399	0.268	0.283	0.295	0.468	0.263	0.245	0.69	0.233	0.138	0.51	0.38	0.217	0.197
Ba	µg/g	49	312	154	186	374	151	215	163	88	154	272	101	510	8	7	520	184	240	*17*
La	µg/g	3.62	4.22	1.04	13.8	3.63	5.15	2.94	2.94	3.31	5.46	2.46	2.60	5.36	2.74	2.06	6.24	3.27	2.40	2.14
Ce	µg/g	6.8	8.2	1.97	28.1	6.70	9.4	4.98	5.09	6.1	10.7	3.98	4.47	10.2	5.37	4.29	12.6	6.1	4.06	3.46
Nd	µg/g	2.8	4.5	*1.2*	17	3.5	4.6	2.9	3.1	3.0	4.5	*1.7*	3.2	5.1	2.8	*2.0*	7	3.3	3.6	*1.3*
Sm	µg/g	0.619	0.79	0.233	2.82	0.71	0.96	0.560	0.550	0.607	0.94	0.424	0.445	1.10	0.506	0.354	1.17	0.627	0.530	0.456
Eu	µg/g	0.136	0.189	0.058	0.614	0.149	0.203	0.117	0.103	0.124	0.192	0.089	0.081	0.246	0.112	0.075	0.246	0.139	0.103	0.102
Tb	µg/g	0.082	0.115	0.075	0.257	0.088	0.145	0.066	0.059	0.076	0.119	0.061	0.047	0.137	0.064	0.045	0.133	0.072	*0.064*	0.069
Yb	µg/g	0.305	0.403	0.55	0.61	0.412	0.66	0.232	0.243	0.277	0.53	0.246	0.169	0.55	*0.186*	*0.159*	0.64	0.246	*0.217*	0.258
Lu	µg/g	0.047	0.066	0.087	0.095	0.065	0.102	0.0363	0.039	0.040	0.082	0.034	0.0251	0.089	0.028	0.022	0.106	0.038	0.037	0.038
Hf	µg/g	1.99	3.41	4.45	4.70	2.91	3.39	1.18	1.90	1.31	3.61	1.34	0.87	3.77	0.70	0.58	4.18	0.76	1.43	0.64
Ta	ng/g	81	101	62	222	79	154	49	59	53	149	49	36	163	42	*23*	179	57	*44*	29
W	ng/g	220	240	140	510	200	280	110	130	100	220	110	60	300	*80*	*60*	300	*80*	*140*	60
Au	ng/g	1.6	1.6	*0.7*	*1.2*	1.9	1.8	0.36	0.9	1.8		*0.5*	*0.3*	*1.4*			1.8	2.1	2.3	0.44
Th	µg/g	0.86	0.87	0.56	2.25	0.83	1.21	0.63	0.67	0.73	1.22	0.63	0.50	1.32	0.60	0.42	1.47	0.76	0.60	0.47
U	µg/g	1.40	1.50	0.89	1.73	0.50	0.91	0.44	0.75	0.38	0.69	0.46	0.48	0.90	*0.24*	*0.15*	0.81	0.38	1.14	0.36

‡This sample from an undocumented location is anomalous in CaO content, likely reflecting secondary calcite cement. The CaO content of most Coconino samples was below the INAA detection limit.

TABLE 3. COMPOSITIONS OF METEOR CRATER IMPACT-MELT PARTICLES DETERMINED BY INAA*.

samples‡		IIG-1a	IIG-1b	IIG-2a	IIG-2b	IIG-3a	IIG-3b	IIG-3c	IIG-3d	IIG-4	SIG-1	SIG-2	SIG-3	SIG-4	M1	M3a	M3b	M4a	M5	M6	M7	M8a	M8b
mass†	mg	83.16	107.47	78.63	98.38	100.52	87.19	20.05	31.29	25.5	9.43	79.08	0.84	27.05	50.34	52.81	50.47	50.93	38.54	48.57	48.94	49.70	63.17
Na	µg/g	433	421	608	496	507	415	464	558	130	240	125	209	179	214	157	150	151	171	284	157	206	384
K_2O	wt%	0.35	0.32	0.38	0.31	0.34	0.32	0.289	0.381	0.134	0.218	0.099	*0.17*	0.353	0.202	0.216	0.201	0.134	0.140	0.26	*0.097*	0.40	0.50
CaO	wt%	*12.1*	*12*	*7.3*	*8*	*10*	9.7	10.4	10.1	16.0	*14*	*13*	13	13.4	14.8	10.0	10.0	14.3	12.8	10.9	13.6	9.1	8.4
Sc	µg/g	2.00	1.98	2.38	2.17	2.19	1.96	2.30	2.47	2.36	1.99	1.89	1.86	1.37	1.50	1.59	1.55	1.74	1.90	2.22	1.69	2.36	2.90
Cr	µg/g	84	84	80	81	83	85	80	80	86	80	91	*91*	84	82	82	84	78	81	79	86	73	72
Fe	mg/g	180	184	178	190	180	184	183	179	210	183	245	202	206	196.2	210.6	215.7	171.5	201.7	163.3	220.5	149.3	135.5
Co	µg/g	910	880	824	910	826	870	828	772	940	870	1030	930	1010	912	960	1000	782	776	722	1020	687	589
Ni	mg/g	14.0	12.6	12.5	14.0	11.5	12.4	11.5	10.4	15.3	14.2	17.7	15.9	16.3	13.7	13.6	14.2	11.9	12.3	9.6	15.9	9.5	8.1
Zn	µg/g														32			28	34	35	33		62
As	µg/g	7.2	6.3	7.1	6.7	6.1	6.0	7.7	6.4	2.58	2.9	13.4	3.6	7.3	5.1	14.3	14.1	2.49	7.6	11.6	2.4	6.6	6.6
Se	µg/g	1.0	0.7		0.8	0.8	0.7	0.7														0.6	
Br	µg/g	0.37	0.31	0.39	*0.32*	0.35	0.35	0.70	0.43	0.45	1.0	0.26	6.8	0.48	0.76	0.74	0.81	0.30	1.0	1.9	*0.21*	0.59	0.65
Rb	µg/g			14	17	16	11	14															20
Sr	µg/g																						
Zr	µg/g	130	150	180	110	160	150	180	240	220	230	180		160	150	150	120	140	210	250	190	170	160
Sb	ng/g	260	230	300	260	230	220	280	260	160	*170*	170		210	170	220	220	110	260	270	120	320	380
Cs	µg/g	0.82	0.81	1.05	0.98	0.91	0.81	0.68	1.05	0.27	0.7			0.74	0.42	0.44	0.41	0.26	0.30	0.62	0.26	1.18	1.53
Ba	µg/g	430	470	540	550	470	500	530	610	300	*190*	270		1960	530	820	810	240	690	410	180	320	300
La	µg/g	13.2	13.9	16.6	17.4	11.6	10.0	19.5	16.6	18.0	9.3	11.7	7.0	5.81	4.90	8.6	8.3	9.0	10.2	13.3	22.2	11.0	15.0
Ce	µg/g	25.7	28.3	34.2	37.7	20.6	17.8	33.6	29.4	42.2	17.1	23.3	21	9.2	9.5	13.3	12.9	14.6	14.2	18.7	23.5	16.9	23.0
Nd	µg/g	*15*	16	21	15	14	14	15	13	16		11			6			11	12	13	24	17	16
Sm	µg/g	2.39	2.50	3.01	3.11	2.06	1.83	3.39	2.98	3.49	1.90	2.33	1.56	1.11	1.06	1.60	1.54	1.80	1.98	2.34	3.75	1.95	2.66
Eu	µg/g	0.57	0.58	0.71	0.73	0.48	0.43	0.78	0.70	0.80	*0.41*	0.57	0.32	*0.23*	0.252	0.38	0.37	0.43	0.47	0.57	0.92	0.46	0.62
Tb	µg/g	0.36	0.41	0.49	0.42	0.32	0.26	0.45	0.39	0.43	*0.35*	0.41		*0.18*	0.15	0.26	0.21	0.26	0.28	0.33	0.53	0.25	0.36
Yb	µg/g	1.04	1.10	1.32	1.27	1.00	0.91	1.44	1.29	1.43	0.97	1.05	0.8	0.68	0.64	0.84	0.75	0.88	1.00	1.16	1.42	0.83	1.06
Lu	µg/g	0.161	0.165	0.197	0.186	0.144	0.138	0.22	0.196	0.201	*0.14*	0.149	0.12	*0.12*	0.091	0.126	0.116	0.125	0.133	0.172	0.194	0.134	0.153
Hf	µg/g	3.86	4.03	4.17	3.72	3.80	3.87	4.5	4.3	5.0	4.6	4.4	3.4	4.7	4.5	4.5	4.2	4.6	5.2	5.9	4.4	4.43	4.9
Ta	ng/g	250	250	250	280	270	240	230	250	360	400	260		230	240	240	220	270	270	270	220	260	280
W	ng/g	400	300	400		350	360	300	200			270		320	280		350			270		290	
Ir	ng/g	450	410	360	410	370	390	410	360	285	360	460	*350*	580	460	530	560	382	448	388	374	359	302
Au	ng/g	160	142	124	150	101	113	87	117	*11*	62	24	37	314	110	251	256	28.7	101	71	50	124	115
Th	µg/g	2.1	2.1	2.4	2.4	2.0	1.81	2.4	2.3	3.3	1.6	2.1	*2.5*	*1.4*	1.43	1.66	1.7	1.7	1.78	2.0	1.6	2.06	2.59
U	µg/g	1.20	1.03	0.86	0.70	0.95	1.69	0.83	0.91	*0.23*	0.87	0.43		1.69	1.10	2.33	2.29	0.39	0.74	0.66	0.71	0.93	1.11

*Note that in this table Ni is given in units of mg/g. Typical 1σ relative uncertainties are: ≤2% - Na, Sc, Fe, Co, Ni, La, Sm; 1-3% - Cr; 1-4% - As, Ce, Eu, Hf, Ir; 1-5% - Yb, Au; 2-6% - K_2O, CaO, Lu; 2-8% - Ba, th; 2-12% - Tb, U; 2-16% - Cs; 4-5% - Sr; 4-12% - Sb; 5-20% - Zn, Br, Ta; 10-35% - Zr; 10-50% - Rb, Nd, W; 25-45% - Se. Values in italics have uncertainties 1.33-3 × the upper end of the typical uncertainty range. Underlined values have uncertainties 3-6 × the upper end of the typical uncertainty range. In all cases, the proper numbers of significant digits are used.

†mass refers to weight in mg of analyzed material and represents most or all of the mass of sample prepared. H11 is an exception; this is a split of homogenized powder prepared by combining 15 impact-melt particles.

‡Samples IIG-1a, IIG-1b etc. and M3a, M3b are different splits of individual impact-melt particles run as homogeneity tests. Sample M8a is hand-picked fresh interior glass, while M8b is fine dust produced during crushing of an individual impact-melt particle. Samples M13a and M13b are respectively exterior and interior sample pairs from an individual impact-melt particle. Samples M18a and M18b are respectively interior and exterior sample pairs from an individual impact-melt particle. H11a is an individual impact-melt particle from the same group as used for sample H11.

TABLE 3. CONTINUED.

		M10	M11	M12	M13a	M13b	M14	M15	M16	M17	M18a	M18b	M19	M21	M23	M24	M22	M26	M27	M20	M25	H11	H11a
mass†	mg	50.33	50.56	44.06	49.01	44.40	47.86	37.00	57.45	29.48	48.89	28.67	25.59	32.17	30.47	33.75	35.20	9.54	22.52	5.10	32.93	78.25	67.24
Na	µg/g	232	411	425	356	204	114	263	166	264	753	841	384	234	200	176	153	167	570	1870	125	299	208
K_2O	wt%	0.32	0.45	1.23	0.26	0.160	0.167	0.52	0.31	0.256	0.49	0.28	0.41	0.169	0.158	0.222	0.154	0.127	0.30	*0.49*	0.079	0.32	0.33
CaO	wt%	12.9	16.0	14.6	8.4	11.1	9.0	18.6	11.1	12.0	18.0	18.4	13.3	17.7	18.2	*10.8*	12.2	15.2	16.1	2.8	13.4	11.2	12.9
Sc	µg/g	1.67	2.17	4.20	2.87	1.84	1.46	1.64	1.83	1.54	1.63	1.75	1.32	2.19	2.07	1.82	3.50	1.74	1.86	3.81	1.66	2.26	1.84
Cr	µg/g	80	58	34.4	87	87	86	58	76	74	51.5	54	58	66	66	86	86	74	67	69	89	78	75
Fe	mg/g	191.3	71.0	42.9	187.4	186.9	181.4	79.5	141.7	151.4	55.2	58.0	97.7	100.3	104.5	192.8	235.0	177.0	129.0	67.0	218.9	173.1	159.9
Co	µg/g	891	311	169	700	785	792	372	584	694	244	248	452	417	435	903	757	733	518	285	1020	763	744
Ni	mg/g	11.3	4.71	2.48	9.0	9.1	11.0	5.8	7.1	9.2	3.87	3.88	6.1	7.2	7.4	13.1	13.2	12.0	8.5	*1.48*	15.9	10.0	9.4
Zn	µg/g		*25*	*16*				15	33		13	18		25			21		21	77		29	101
As	µg/g	5.3	5.4	*0.28*	28.9	11.7	14.1	1.52	8.0	19.4	2.95	3.36	7.0	6.5	5.70	12.4	30.2	6.2	5.4	13.4	4.4	7.6	5.2
Se	µg/g	1.2					0.9						0.7										0.6
Br	µg/g	0.8	2.4	*0.10*	4.4	3.4	1.7	1.23	3.2	2.2	1.24	2.0	1.40	0.60	0.40	0.65	0.53	0.73	0.32	5.0	0.36	1.1	0.57
Rb	µg/g	16	15	39				18	11		17	10	16						8				
Sr	µg/g										580	640								350			
Zr	µg/g	160	230	320	190	190	110	200	260	200	240	220	190	160	180	190	310	210	230	500	160	150	160
Sb	ng/g	190	310	150	440	220	220	150	370	160	160	90	160	140	100	310	260	*130*	170	*130*	*80*	260	200
Cs	µg/g	0.63	1.01	3.23	0.53	0.27	0.52	0.92	0.52	0.44	0.85	0.50	0.67	0.44	0.29	0.49	0.24	0.25	0.52	0.56	0.21	0.78	0.65
Ba	µg/g	930	470	273	600	430	270	580	420	4900	10100	13400	6400	200	220	470	390	320	690	2110	160	540	670
La	µg/g	8.0	7.87	14.6	23.1	10.6	5.23	7.83	13.2	4.69	6.75	5.44	4.83	9.1	6.05	10.6	24.6	8.3	7.83	9.0	6.62	12.2	7.86
Ce	µg/g	13.9	14.6	28.1	27.8	14.0	9.8	12.3	18.3	9.3	11.6	11.1	9.0	19.5	18.8	19.1	47.3	13.0	13.7	25.9	10.8	22.4	14.3
Nd	µg/g	11	7	13	24	13		7	14	8	6	7		11	6	10	29		6		5	13	
Sm	µg/g	1.48	1.50	2.98	4.63	1.97	1.06	1.47	2.47	1.04	1.33	1.23	0.98	2.08	1.46	1.98	6.23	1.72	1.64	1.92	1.43	2.33	1.54
Eu	µg/g	0.34	0.341	0.65	1.11	0.47	0.246	0.322	0.59	0.239	0.304	0.288	0.226	0.50	0.350	0.47	1.51	0.41	0.37	0.43	0.36	0.54	0.354
Tb	µg/g	0.20	0.215	0.419	0.65	0.29	0.15	0.202	0.36	0.15	0.203	0.185	0.14	0.30	0.22	0.27	0.93	0.24	0.24	0.32	0.21	0.34	0.22
Yb	µg/g	0.83	0.86	1.62	1.85	1.02	0.65	0.88	1.15	0.65	0.82	0.76	0.66	0.95	0.85	0.94	2.30	1.03	0.90	1.18	0.72	1.095	0.94
Lu	µg/g	0.135	0.138	0.248	0.258	0.145	0.096	0.146	0.167	0.107	0.122	0.114	0.103	0.146	0.126	0.139	0.334	0.146	0.139	0.17	0.102	0.163	0.141
Hf	µg/g	5.2	5.9	8.3	5.9	4.9	4.4	5.3	6.6	4.98	6.1	6.2	5.3	5.2	5.6	4.7	6.6	4.8	5.5	13.4	3.92	5.1	5.1
Ta	ng/g	220	270	520	260	200	220	240	260	210	270	290	220	310	290	240	340	*210*	240	570	200	240	230
W	ng/g	600	400	570	410	220	200	290	200	400	380	260	320	190	190		440			400			500
Ir	ng/g	479	169	2.4	421	405	437	133	321	433	93	101	255	160	183	518	400	403	259	91	485	380	350
Au	ng/g	164	85	2.3	157	139	202	21.7	112	180	19.8	15.1	122	*7.0*	*4.0*	243	24.5	40	25.9		57	124	93
Th	µg/g	1.6	1.93	4.05	3.3	1.74	1.35	1.66	1.8	1.44	1.70	1.76	1.35	2.12	2.03	1.81	5.3	1.62	1.75	3.9	1.36	2.31	1.8
U	µg/g	1.6	1.57	1.91	0.55	0.53	1.13	2.08	0.33	1.52	1.98	1.31	1.85	0.32	0.32	0.78	0.66	0.77	0.89	0.88	0.26	1.28	1.65

TABLE 4. MAJOR-ELEMENT COMPOSITIONS OF IMPACT-MELT PARTICLES DETERMINED BY EMPA OF FUSED BEADS

	IIG-1a	IIG-2a	IIG-3a	IIG-4	M1	M3	M4	M7	M8	M10
SiO_2	47.9	51.8	50.9	41.7	43.0	47.7	43.4	45.3	54.4	47.6
TiO_2	0.19	0.20	0.18	0.22	0.17	0.19	0.18	0.19	0.20	0.23
Al_2O_3	3.10	3.47	3.30	3.41	2.54	3.04	2.74	2.92	3.88	3.23
Cr_2O_3	0.01	0.02	0.01	0.01	0.01	0.02	0.02	0.02	0.01	0.01
FeO	25.3	27.4	25.5	22.7	26.3	28.4	24.7	27.7	20.9	25.2
MnO	0.12	0.17	0.10	0.12	0.03	0.07	0.05	0.05	0.06	0.06
MgO	8.67	5.93	7.83	12.0	10.7	9.44	10.9	9.06	8.60	8.70
CaO	13.6	9.38	11.0	19.2	16.6	10.4	17.4	13.8	11.1	14.0
Na_2O	0.07	0.08	0.07	0.02	0.03	0.03	0.03	0.05	0.03	0.05
K_2O	0.39	0.42	0.37	0.19	0.19	0.27	0.15	0.21	0.42	0.42
P_2O_5	0.74	1.14	0.63	0.47	0.35	0.43	0.44	0.77	0.37	0.46

	M11	M13	M14	M15	M16	M17	M18	M19	SIG-4
SiO_2	55.6	50.0	51.9	52.0	51.9	52.1	54.5	57.9	44.6
TiO_2	0.24	0.22	0.16	0.20	0.26	0.18	0.21	0.16	0.18
Al_2O_3	3.40	3.19	2.70	2.95	3.24	2.79	3.25	2.68	2.86
Cr_2O_3	0.01	0.02	0.02	0.01	0.05	0.01	0.01	0.01	0.02
FeO	9.05	26.0	24.9	11.3	20.3	20.7	7.93	12.7	30.3
MnO	0.07	0.09	0.05	0.08	0.11	0.03	0.04	0.03	0.07
MgO	12.4	8.78	9.09	13.2	10.6	10.2	13.8	11.1	8.47
CaO	18.5	11.0	10.7	19.4	12.8	13.3	19.5	14.7	12.5
Na_2O	0.06	0.06	0.03	0.04	0.03	0.04	0.12	0.06	0.03
K_2O	0.43	0.29	0.21	0.32	0.38	0.26	0.39	0.37	0.38
P_2O_5	0.25	0.38	0.30	0.48	0.30	0.33	0.33	0.31	0.58

TABLE 5. COMPOSITIONS OF METALLIC SPHERULES AND THE REMBANG IVA IRON DETERMINED BY INAA*.

Spherule #		1	2	3	4	5	6	7	8	9	10	11	12	14
mass	(mg)	9.03	12.58	8.53	9.35	11.24	3.32	12.83	8.60	9.40	5.08	3.96	4.36	2.12
Fe	mg/g	818	716	815	714	800	570	768	740	772	834	759	637	614
Co	mg/g	7.6	9.3	8.9	5.6	9.1	7.5	10.4	11.1	10.0	7.3	10.7	3.1	3.2
Ni	mg/g	128	152	152	86.6	148	124	169	181	166	115	171	50.2	38.9
Ga	µg/g	92.3†	88.2†	120	83.5†	110	170	81.8†	-	50	-	-	80	90
Ge	µg/g	514†	772†	-	485†	-	-	795†	-	-	-	-	-	-
As	µg/g	44.1	49.5	48.0	24.0	48.2	66.8	51.9	63.8	52.1	25.8	64.9	19.0	27.5
Ir	µg/g	4.48	5.53	5.4	3.14	4.9	9.15	6.07	6.62	5.83	4.18	6.75	2.61	1.96
Au	µg/g	3.17	3.85	3.86	2.11	3.74	1.99	4.3	4.57	4.26	2.72	4.69	1.28	0.63
Σ(Fe, Co, Ni)		954	877	976	806	957	702	947	932	948	956	941	690	656

Spherule #		15	16	17	18	19	20	21	23	Rembang‡			
										this work	WR01	WR01	S96
mass	(mg)	5.21	5.24	0.72	3.25	9.39	3.80	2.21	2.38	16.7			
Fe	mg/g	820	748	676	783	726	745	653	788	943	-	-	-
Co	mg/g	8.0	11.3	3.3	9.7	12.6	9.6	2.8	7.7	4.0	4.03	4.03	4
Ni	mg/g	130	182	41.1	155	216	164	31.3	137	89.6	85.4	88.4	-
Ga	µg/g	-	-	-	-	-	-	-	-	-	-	-	-
Ge	µg/g	-	-	-	-	-	-	-	-	-	-	-	-
As	µg/g	41.7	94.9	20.7	47.9	84.8	44.4	13.7	43.0	9.4	8.85	8.93	9
Ir	µg/g	4.73	6.77	2.24	5.69	7.57	5.76	1.59	5.09	1.19	1.16	1.16	1.14
Au	µg/g	3.51	4.57	0.75	4.11	5.59	4.09	0.55	3.58	1.19	1.78	1.75	1.91
Σ(Fe, Co, Ni)		958	941	720	948	955	919	687	933	1037			

*Typical INAA 1σ relative uncertainties are: 1% - Fe, Co; 2% - Au; 1-3% - Ni; 2-4% - Ir; 5-10% - As; 30-50% - Ga.
†These analyses done by RNAA, typical 1σ relative uncertainties are 4%.
‡WR01 – Wasson and Richardson (2001); S96 – Scott et al. (1996).

FIGURE CAPTIONS

Figure 1. Variation in major-element compositions of Meteor Crater target rocks with depth demonstrating the unique geochemical characteristics of the different formations. On this and all subsequent figures, the data are adjusted to a volatile- and Fe-free basis to correct for differences in CO_2 and H_2O in the target rocks, and differences in projectile components in impact-melt particles. See text for a discussion of the rationale for adjusting the data. Note that Mg and Ti are plotted on log scales. Data from See et al. (2002).

Figure 2. Variation in trace-element compositions of Meteor Crater target rocks with depth demonstrating the unique geochemical characteristics of the different formations.

Figure 3. Major-element variation diagrams comparing Meteor Crater target rocks with impact-melt particles demonstrating that the Moenkopi and Kaibab Formations are the major target-rock contributors to the impact-melt particles. The inset in the Mg vs. Al diagram shows that mixing of at most 10% of Coconino Formation could be hidden in the scatter of the data, but no Coconino or Toroweap components are required by the data. Some target-rock data from See et al. (2002).

Figure 4. Ca vs. Sc, Ca vs. Ta, and Ta vs. Sc diagrams comparing Meteor Crater target rocks with impact-melt particles, further demonstrating that the Moenkopi and Kaibab Formations are the major target-rock contributors to the impact-melt particles.

Figure 5. Ca vs. trace-element diagrams comparing Meteor Crater target rocks with impact-melt particles. Secondary mineral data are from Appendix 3.

Figure 6. Element-element diagrams for siderophile elements in Meteor Crater impact-melt particles, showing data for impact-melt particles from Wabar Crater (Mittlefehldt et

al., 1992) and Wolfe Creek Crater (Attrep et al., 1991) for comparison. The data are normalized to the projectile composition. The Meteor Crater samples have Co/Ni and Ir/Ni ratios equivalent to the Canyon Diablo iron, but show strong fractionations in Au/Ir.

Figure 7. Co vs. Au/Ni for impact-melt particles. Particles covering nearly the entire rage in Au/Ni ratios can have similar Co contents, and samples with similar Au/Ni can have substantially different Co contents. Thus the Au/Ni fractionation is not related to the mixing ratio of projectile and target materials.

Figure 8. Au/Ir vs. (Ca+Mg)/Si of impact-melt particles shows that those particles with a high dolomite component tend to have lower Au/Ir ratios. Br vs. (Ca+Mg)/Si of target rocks shows that the halide Br is roughly correlated with the dolomite content of the target rock. Together, these suggest that volatilization of Au-halides may be responsible for the observed fractionation.

Figure 9. Variations in (Ca+Mg)/Si and (Ca+Mg)/Al with depth in target rocks (left) and with Ir content in impact-melt particles (right). Dashed lines labeled K mark the lower limits of (Ca+Mg)/Si and (Ca+Mg)/Al observed for Kaibab samples, while the line labeled M marks the upper limit of (Ca+Mg)/Si in Moenkopi samples – all Moenkopi samples have (Ca+Mg)/Al <3.

Figure 10. Siderophile-element data for metallic spherules compared to the Canyon Diablo iron. Most spherules have Fe and Ni contents that follow a trend of Fe loss (arrow, upper diagram). Some samples with low Fe are consistent with dilution by oxides. Equivalent normalized Fe contents for hematite, goethite and limonite are shown for comparison. Co-Ni, Ir-Ni and Au-Ni are highly correlated, with most samples

enriched in these elements compared to the Canyon Diablo iron. Dashed lines are regression lines through the Co-Ni and Au-Ni data. The slopes of these lines are consistent with expectations from a simple oxidation model (see text). The metallic spherules show enrichments in As that are inconsistent with a simple oxidation model, but closely mimic the P-Ni trend. This suggests that some selective melting of schreibersite-troilite-rich regions of Canyon Diablo may have occurred (see text). Some data are taken from Blau et al. (1973) and Xue et al. (1995).

Figure 11. Schematic diagrams indicating two possible mechanisms for formation of impact-melt particles at Meteor Crater. Jetting occurs at the point of contact between the projectile and target where they meet in oblique angles. Jetting will occur only until the projectile penetrates to a depth approximately equal to its radius (Melosh, 1989). Based on estimates of the pre-impact stratigraphy and projectile size, the thickness of the Moenkopi may have been roughly ½ the projectile radius. Thus jetting ought to have produced some impact-melt particles composed dominantly of Moenkopi plus meteorite. We have not found any of these, but the compositions of some melts indicate formation at shallow levels of the target. Impact-melts will also form at the interface between the deforming projectile and the transient crater wall, and the melt zone will extend a few projectile radii below the surface (Melosh, 1989). Flow of the melt up the transient crater wall will promote mixing. The data suggest that many of the particles were formed by this latter mechanism.

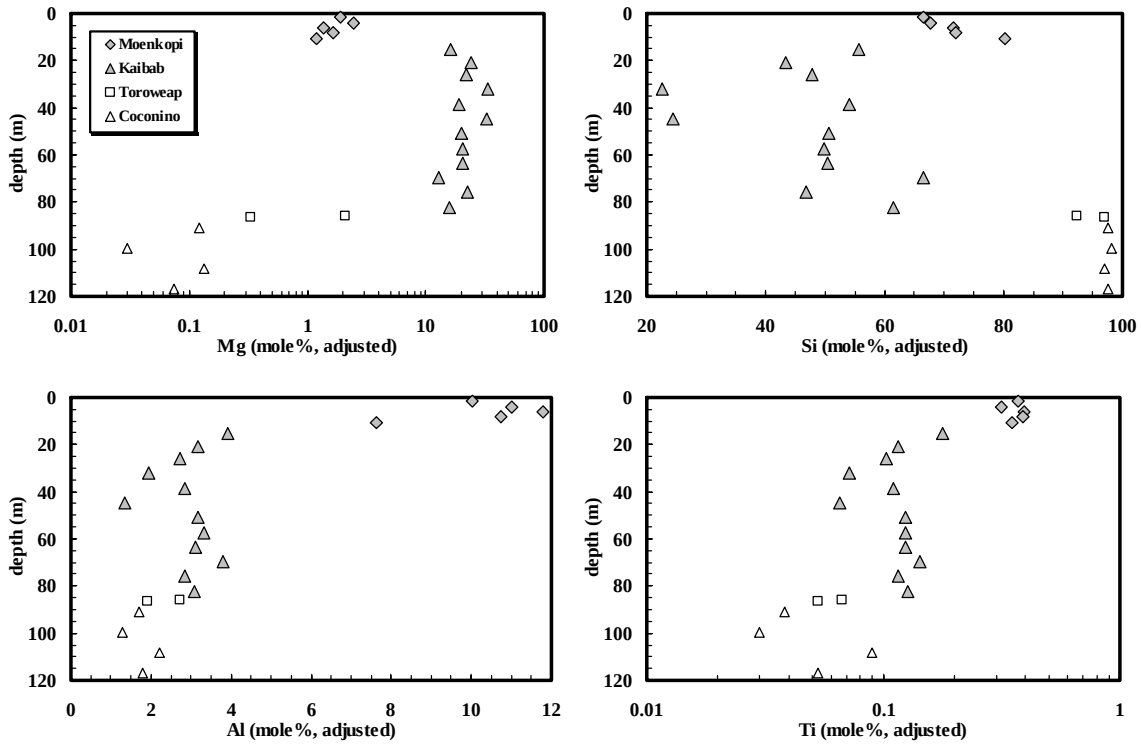
Moenkopi
Kaibab
Toroweap
Coconino
depth (m)
Mg (mole%, adjusted)
Si (mole%, adjusted)
Al (mole%, adjusted)
Ti (mole%, adjusted)

Figure 1

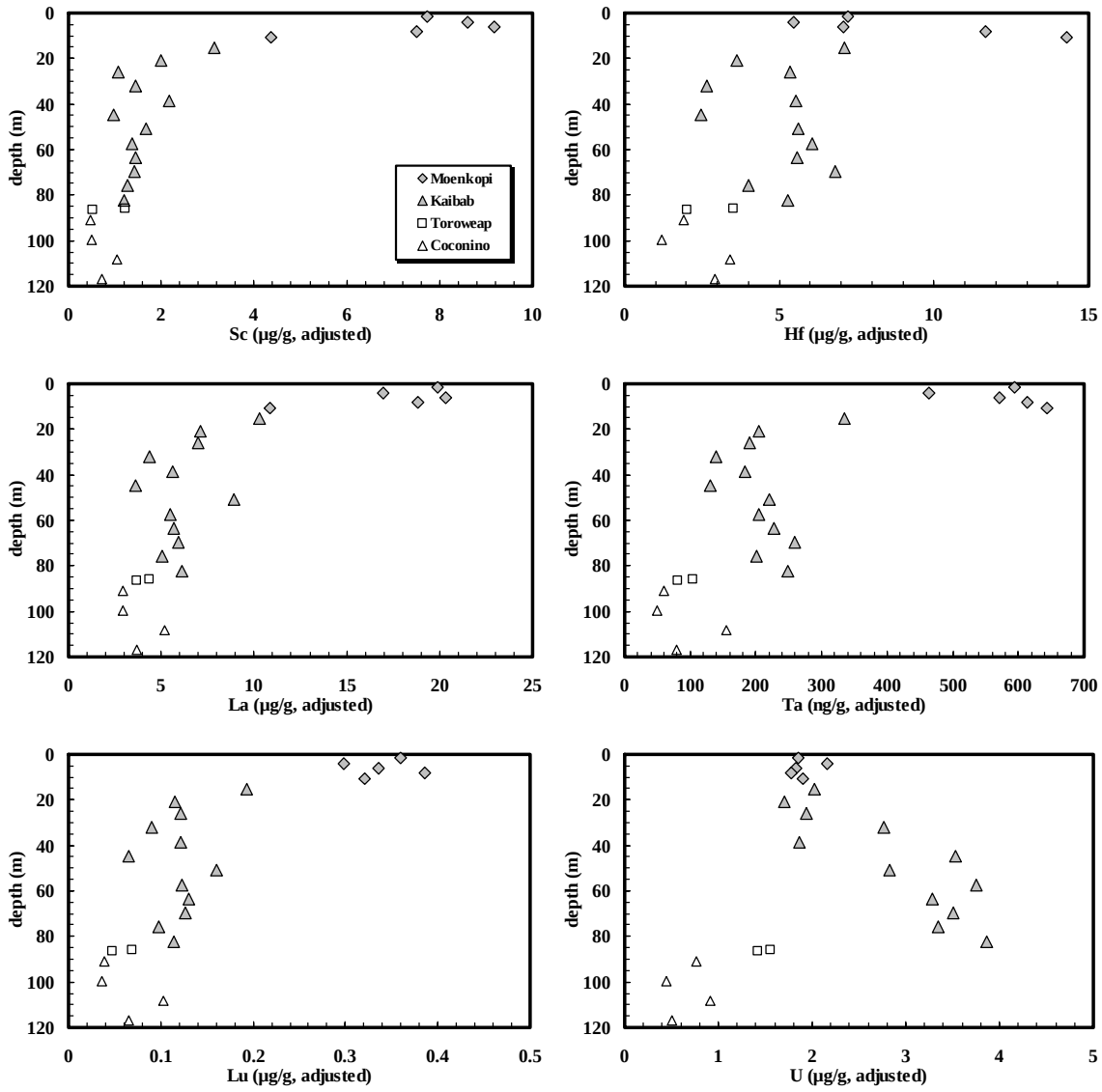
depth (m)
Sc (µg/g, adjusted)
Hf (µg/g, adjusted)
La (µg/g, adjusted)
Ta (ng/g, adjusted)
Lu (µg/g, adjusted)
U (µg/g, adjusted)
Moenkopi
Kaibab
Toroweap
Coconino

Figure 2

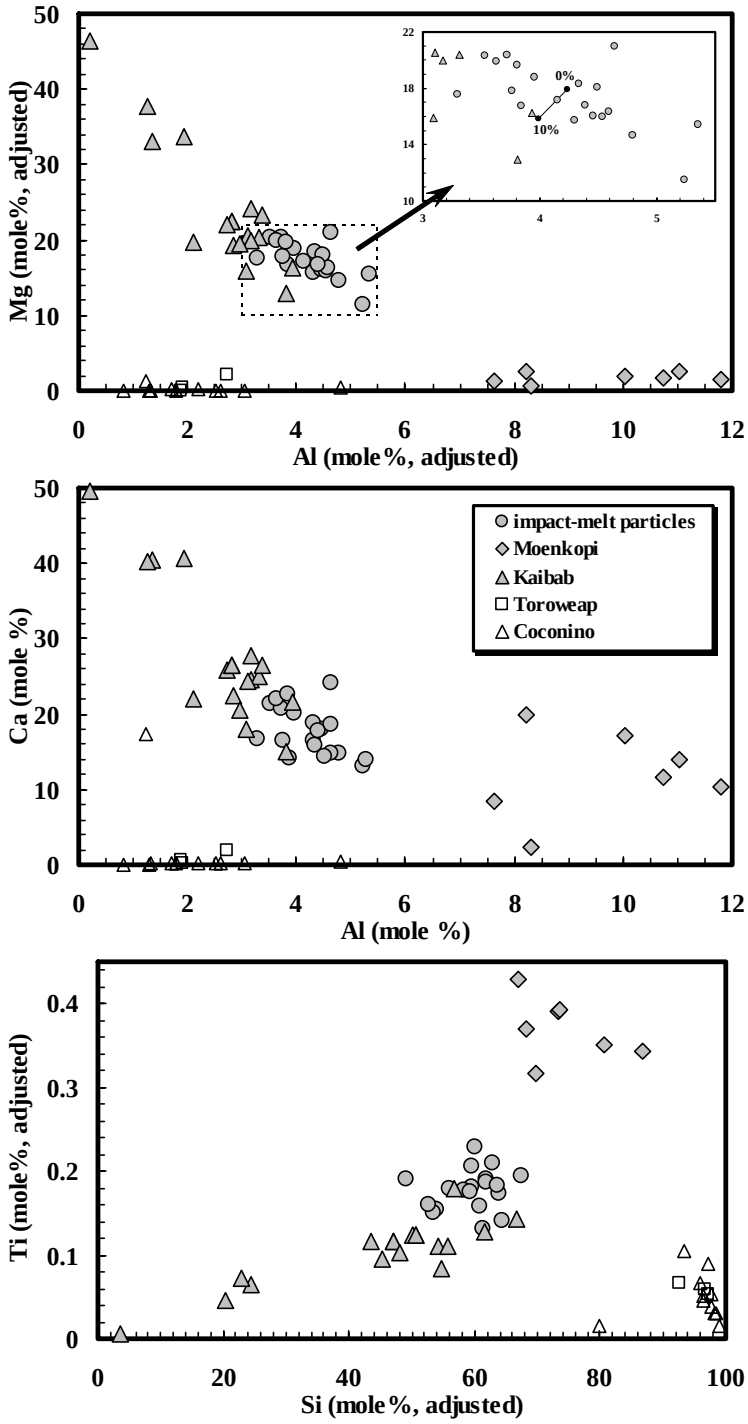
Mg (mole%, adjusted)
Al (mole%, adjusted)
0%
10%
Ca (mole %)
Al (mole %)
impact-melt particles
Moenkopi
Kaibab
Toroweap
Coconino
Ti (mole%, adjusted)
Si (mole%, adjusted)

Figure 3

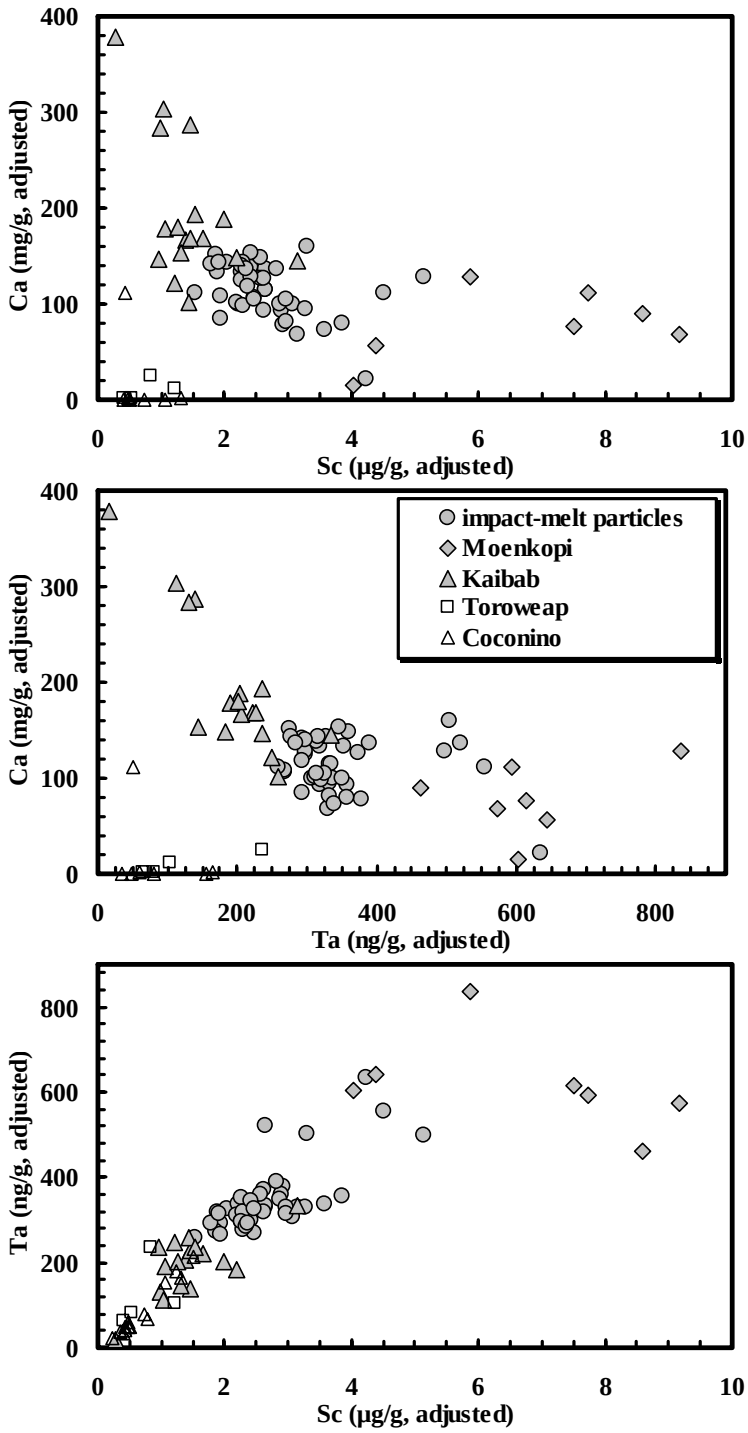
Ca (mg/g, adjusted)
Sc (µg/g, adjusted)
Ca (mg/g, adjusted)
Ta (ng/g, adjusted)
Ta (ng/g, adjusted)
Sc (µg/g, adjusted)
impact-melt particles
Moenkopi
Kaibab
Toroweap
Coconino

Figure 4

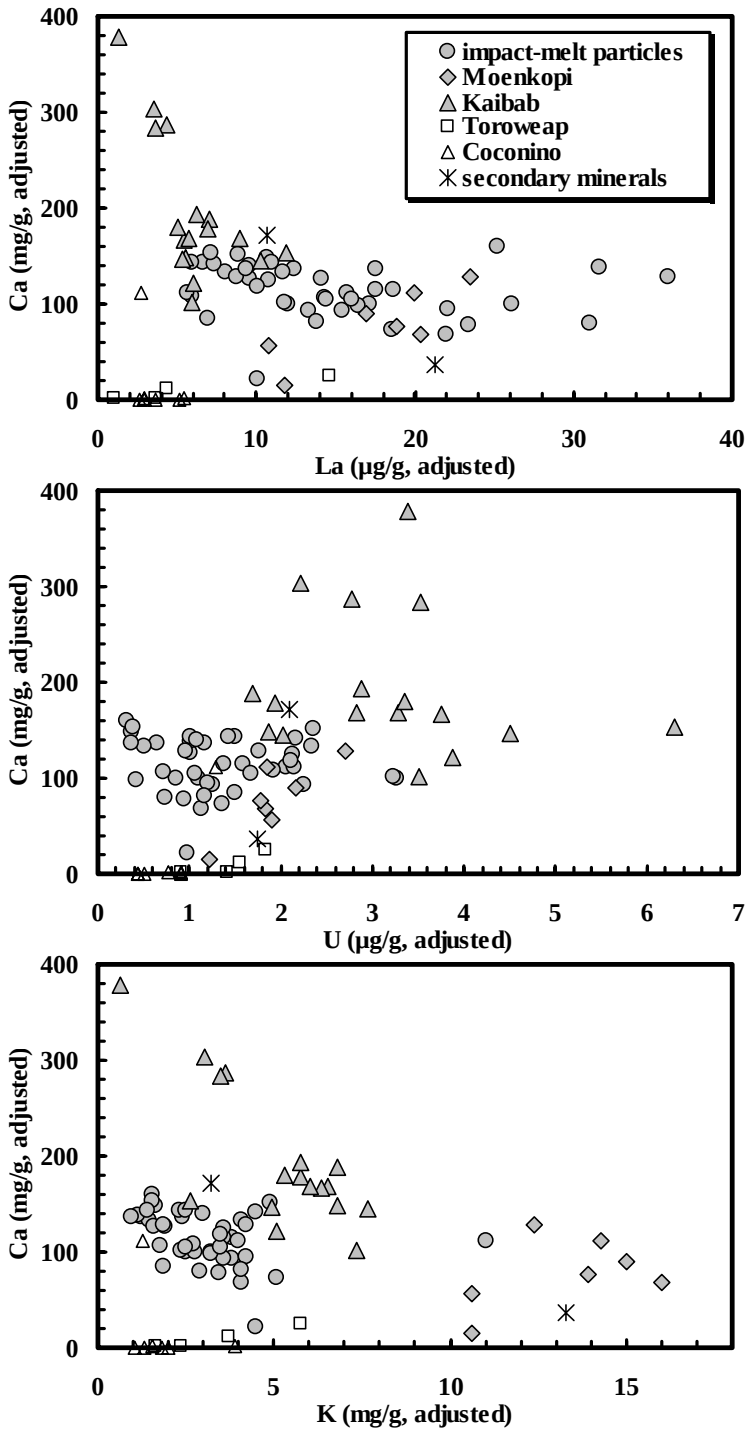
impact-melt particles
Moenkopi
Kaibab
Toroweap
Coconino
secondary minerals
Ca (mg/g, adjusted)
La (µg/g, adjusted)
U (µg/g, adjusted)
K (mg/g, adjusted)
0
100
200
300
400
0
10
20
30
40
1
2
3
4
5
6
7
5
10
15

Figure 5

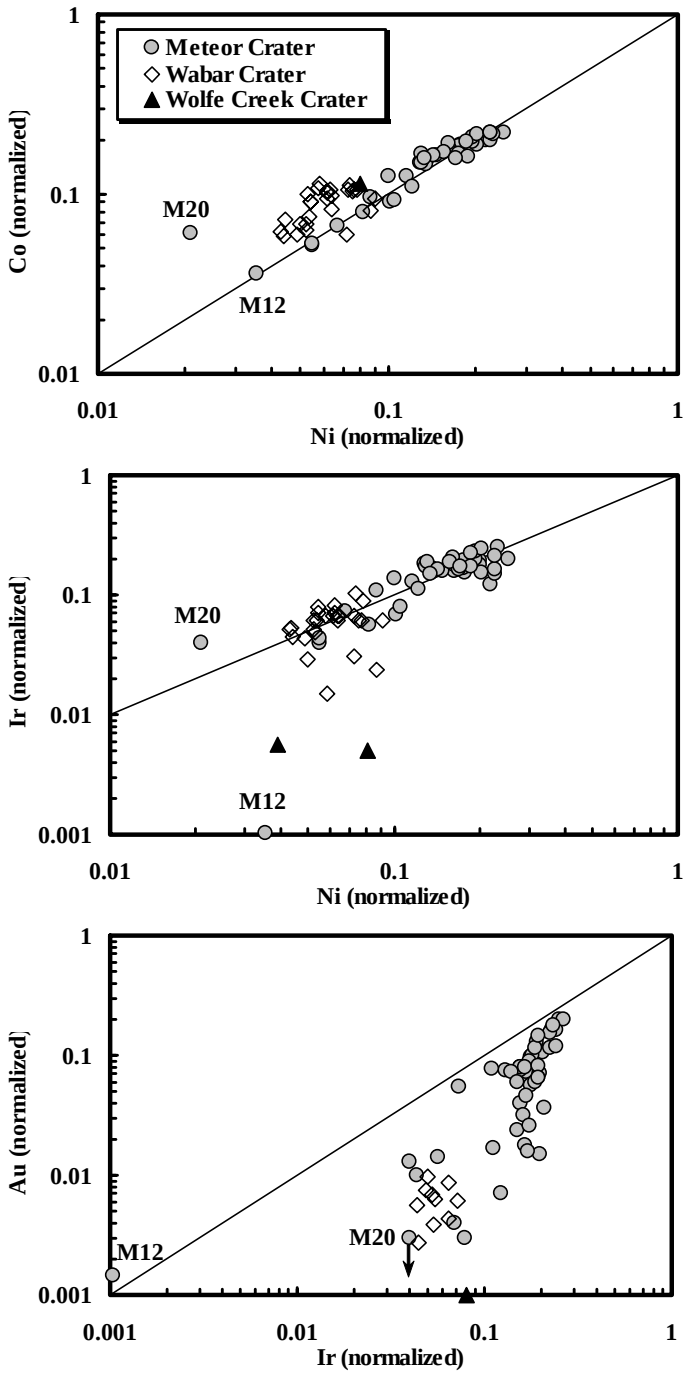
Meteor Crater
Wabar Crater
Wolfe Creek Crater
M20
M12
Co (normalized)
Ni (normalized)
Ir (normalized)
Au (normalized)
1
0.1
0.01
0.001

Figure 6

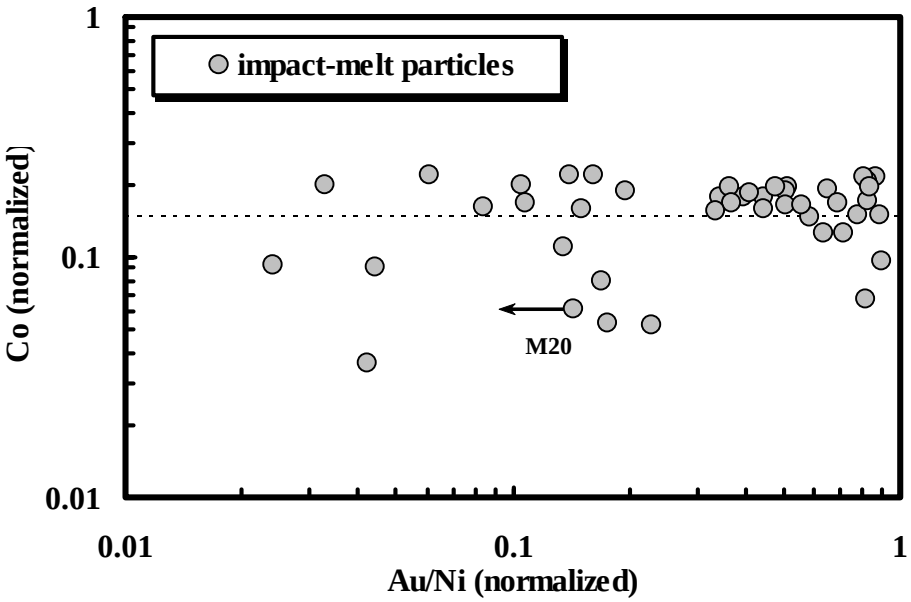
impact-melt particles
M20
Co (normalized)
Au/Ni (normalized)
1
0.1
0.01
0.01
0.1
1

Figure 7

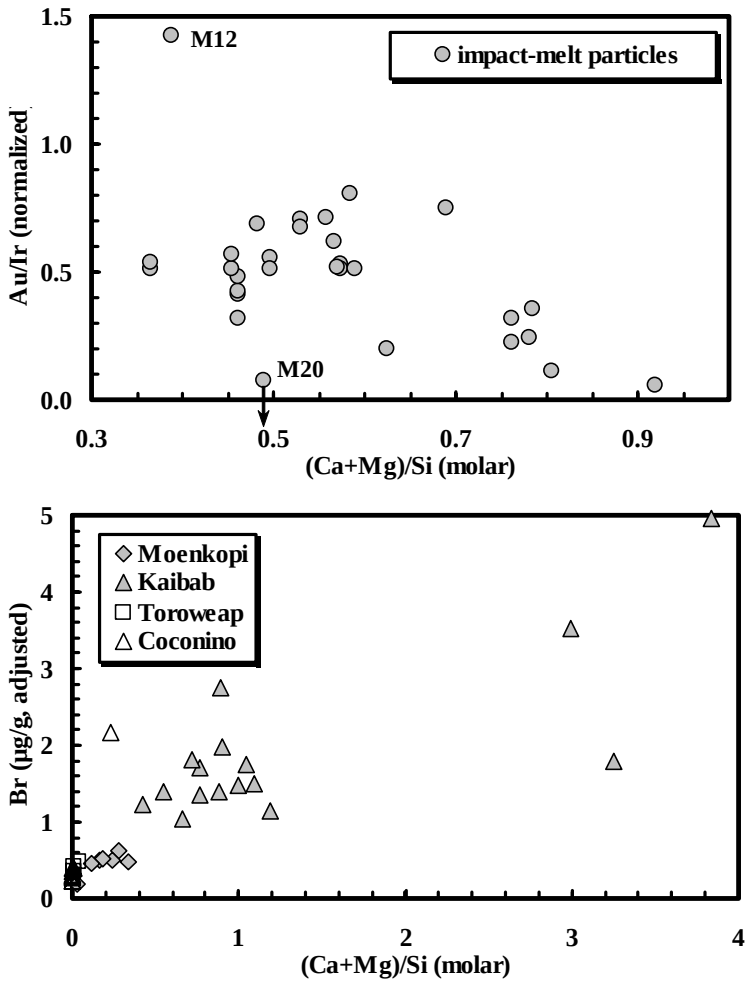
1.5
1.0
0.5
0.0
Au/Ir (normalized)
M12
impact-melt particles
M20
0.3
0.5
0.7
0.9
(Ca+Mg)/Si (molar)
5
4
3
2
1
0
Br (µg/g, adjusted)
Moenkopi
Kaibab
Toroweap
Coconino
0
1
2
3
4
(Ca+Mg)/Si (molar)

Figure 8

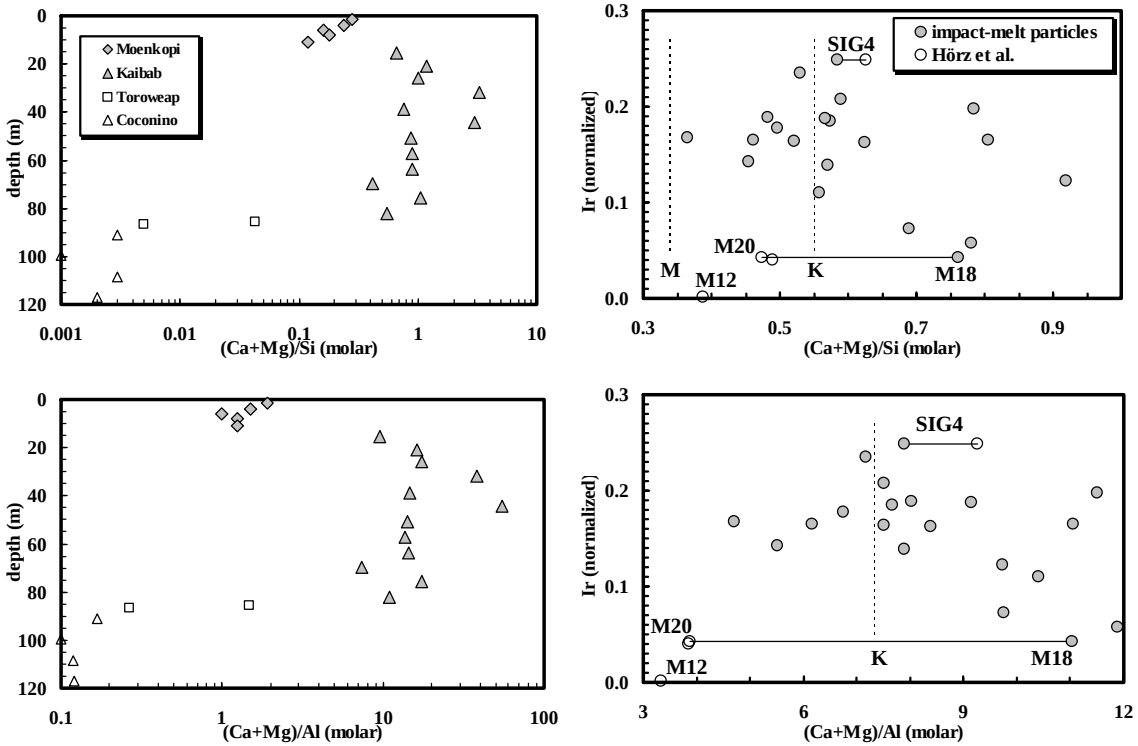
depth (m)
(Ca+Mg)/Si (molar)
Moenkopi
Kaibab
Toroweap
Coconino
Ir (normalized)
impact-melt particles
Hörz et al.
SIG4
M20
M
M12
K
M18
(Ca+Mg)/Al (molar)

Figure 9

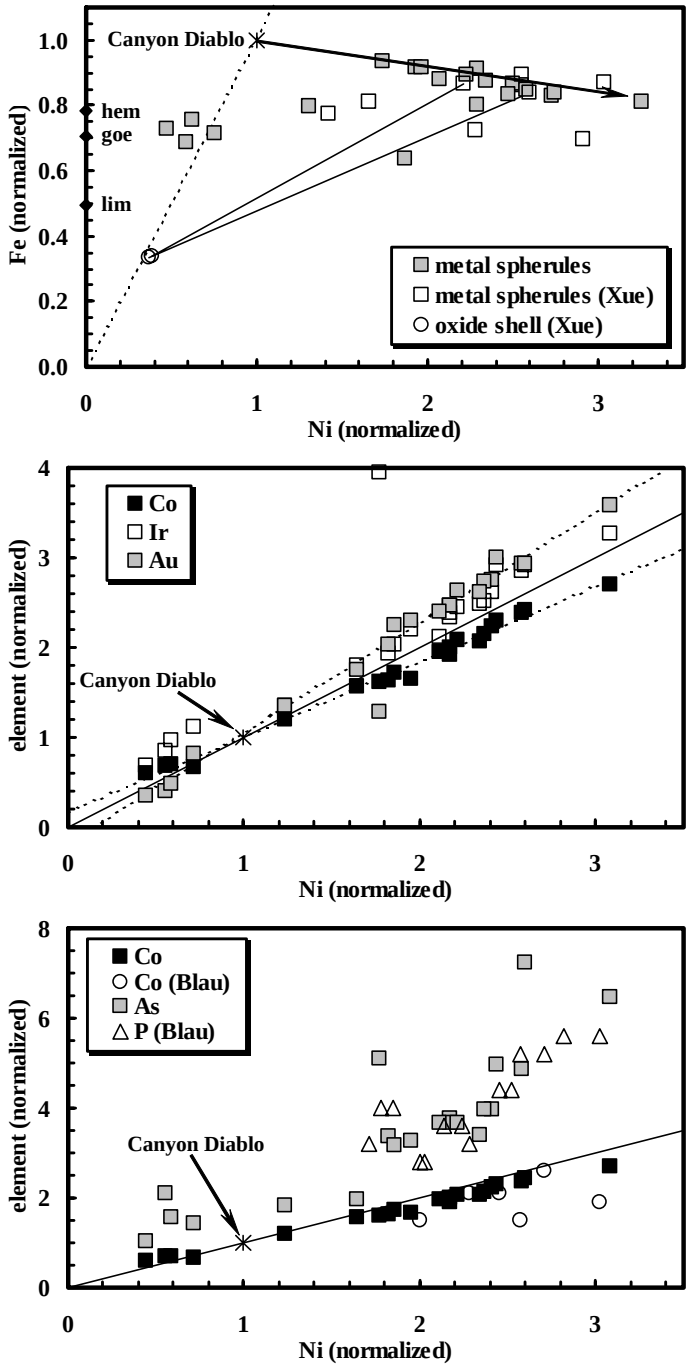
Canyon Diablo
hem
goe
lim
Fe (normalized)
Ni (normalized)
metal spherules
metal spherules (Xue)
oxide shell (Xue)
Co
Ir
Au
element (normalized)
Co
Co (Blau)
As
P (Blau)

Figure 10

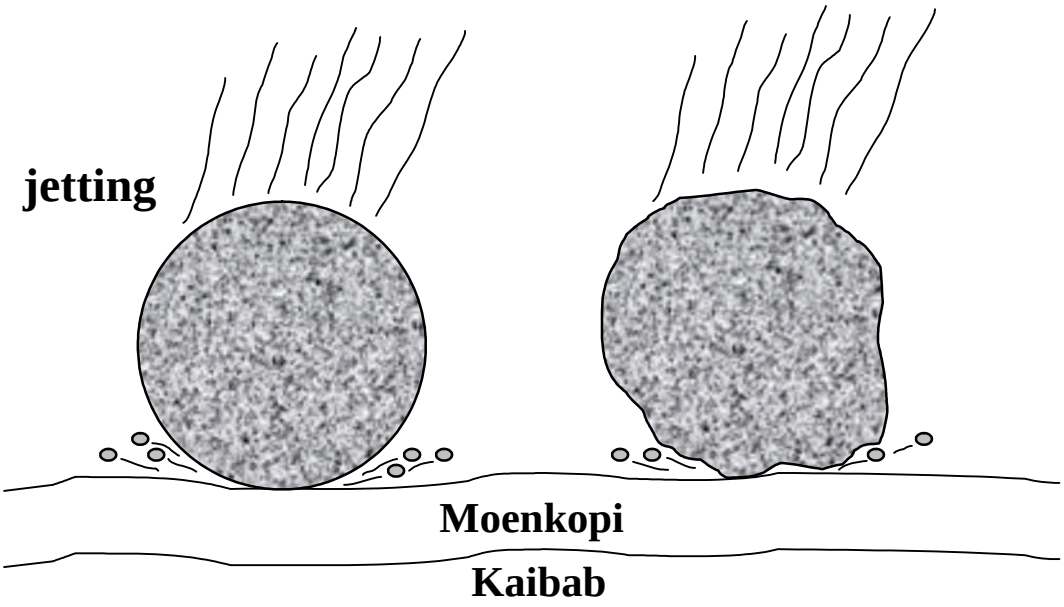
jetting
Moenkopi
Kaibab

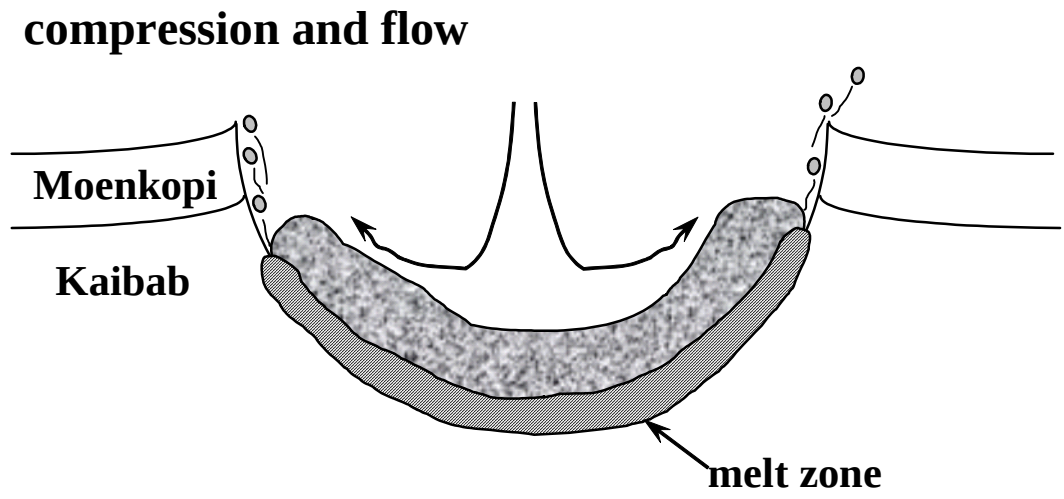
compression and flow
Moenkopi
Kaibab
melt zone

Figure 11